

1

2

3

4

Cosmic ray validation of electrode positions in small-strip thin gap chambers for the upgrade of the ATLAS detector

5

Lia Formenti

6

7

8

Department of Physics
McGill University, Montreal
October, 2021

9

10

11

12

13

A thesis submitted to
McGill University
in partial fulfillment of the
requirements of the degree of
Master of Science

¹⁵ Table of Contents

¹⁶	1	Introduction	1
¹⁷	2	High energy particle physics	4
¹⁸	2.1	The Standard Model	4
¹⁹	2.2	Beyond the Standard Model	6
²⁰	2.3	Studying high energy particle physics with accelerators	7
²¹	3	The LHC and the ATLAS experiment	9
²²	3.1	The Large Hadron Collider	9
²³	3.2	The High-Luminosity LHC	10
²⁴	3.3	The ATLAS experiment	12
²⁵	4	The New Small Wheels	17
²⁶	4.1	Motivation for the New Small Wheels	17
²⁷	4.2	Design of the NSWs	20
²⁸	4.3	Small-strip thin gap chambers	20
²⁹	4.4	sTGC Quadruplet Construction	23
³⁰	4.5	NSW alignment	24
³¹	5	Using cosmic muons to measure relative strip position offsets	27
³²	5.1	Cosmic rays	27
³³	5.2	Experimental setup	28

34	5.3 Data acquisition	29
35	5.4 Data preparation	30
36	5.4.1 Data quality cuts on electrode hits	30
37	5.4.2 Clustering and tracking	30
38	5.5 Relative local offsets	32
39	5.6 Systematic uncertainty	38
40	5.7 Discussion	39
41	6 Using x-rays to measure relative strip position offsets	41
42	6.1 Experimental setup	41
43	6.2 Data acquisition	42
44	6.3 Data preparation	43
45	6.4 Measuring local offsets	43
46	6.5 Measuring relative local offsets	44
47	7 Comparing cosmic muon and x-ray relative strip position offsets	47
48	7.1 Assessing correlation	47
49	7.2 Discussion	52
50	8 Outlook and summary	54
51	8.1 Outlook	54
52	8.2 Summary	55
53	References	56
54	APPENDICES	63
55	A Cluster position uncertainty	64
56	B Analysis statistics	66

57	C Analysis systematics	68
58	C.1 Residual distribution fit function	68
59	C.2 Cosmic muon data collection voltage	71
60	C.3 Cluster fit algorithm	72
61	C.4 Differential non-linearity	73
62	D Printable plots	76

Abstract

64 The Large Hadron Collider (LHC) is used to generate subatomic physics processes at the
65 energy frontier to challenge our understanding of the Standard Model of particle physics.
66 The particle collision rate at the LHC will be increased up to seven times its design value in
67 2025-2027 by an extensive upgrade program. The innermost endcaps of the ATLAS muon
68 spectrometer consist of two wheels of muon detectors that must be replaced to maintain
69 the muon momentum resolution in the high-rate environment. The so-called New Small
70 Wheels (NSWs) are made of two detector technologies: micromegas and small-strip thin gap
71 chambers (sTGCs). The sTGCs are gas ionization chambers that hold a thin volume of gas
72 between two cathode boards. One board is segmented into copper readout strips of 3.2 mm
73 pitch that are used to precisely reconstruct the coordinate of a passing muon. Modules of
74 four sTGCs glued together into quadruplets cover the NSWs. Quadruplets were designed
75 to achieve a 1 mrad angular resolution to fulfill the spectrometer's triggering and precision
76 tracking requirements. To achieve the required angular resolution the absolute position of
77 the readout strips must be known in the ATLAS coordinate system to within 100 μm . At
78 McGill University, the performance of sTGC quadruplets was characterized using cosmic ray
79 data before being sent to CERN, where the charge profile left by x-rays is used to measure
80 the offset of the strip patterns with respect to nominal at a limited number of points on
81 the surface of each quadruplet. The x-ray strip position measurements have acceptable but
82 limited precision and do not span the whole area of the strip layers. Given the importance of
83 knowing the absolute position of each readout strip to achieve the performance requirements
84 of the NSWs, the x-ray method must be validated by an independent method. Cosmic ray
85 data is used to characterize the relative alignment between layers and validate the x-ray
86 method.

Résumé

Le grand collisionneur des hadrons (LHC) utilise des collisions de protons afin de générer des processus de la physique subatomique à la frontière même de la haute énergie, et ceci afin de tenter remettre en cause le modèle standard de la physique des particules. Le taux des collisions entre protons au LHC sera augmenté jusqu'à sept fois le taux nominal d'ici 2025-2027 à l'aide d'un programme de mise à niveau de grande envergure. Une partie du spectromètre à muons du détecteur ATLAS consistant de deux roues de détecteurs de muons doit être remplacée afin de maintenir la résolution sur l'inertie des muons à haut taux de collision. Appelées les Nouvelles Petites Roues (NSWs), elles utilisent deux technologies de détection différentes: des chambres micromegas et des chambres à petites bandes et à intervalles fins (sTGCs). Les sTGCs sont des chambres d'ionisation de gaz, qui contiennent un volume très fin de gaz entre deux panneaux cathodiques. Un panneau est segmenté avec de petites bandes en cuivre en pente de 3.2 mm. Ceux-ci détectent le signal laissé par des muons et permettent la mesure précise des coordonnées spatiales des muons qui traversent le détecteur. Des modules de quatre sTGCs collés ensemble en quaduplets couvrent la superficie des NSWs. Ces quadruplets ont été conçus afin de permettre une résolution angulaire de 1 mrad, et de satisfaire les exigences des systèmes de déclenchement et de mesures de précision. Afin d'atteindre cette résolution angulaire il faut que la position absolue de chaque bande soit connue au sein du détecteur ATLAS avec une précision d'au moins 100 μ m. À l'Université de McGill, la performance des quadruplets a été caractériser avec des rayons cosmiques avant leur envoi au CERN, où le profil des charges laissé par des rayons X est utilisé pour mesurer le déplacement du motif des bandes par rapport à leur emplacement nominal. Ceci est fait à un nombre de positions limité sur la surface des quadruplets. Ces déplacements, mesurés par les rayons X, ont une précision acceptable mais limitée et ne couvrent pas la région entière des panneaux. Étant donné l'importance de la caractérisation précise de la position absolue de chaque bande afin de réaliser les exigences de rendement des NSWs, une méthode indépendante de validation de la méthode des rayons X est requise. Les données recueillies avec les rayons cosmiques sont utilisées pour caractériser l'alignement relatif entre les panneaux et valider la méthode des rayons-X.

Acknowledgements

- 117 Experimental particle physics projects are never done alone. I am grateful to have been
118 working with the ATLAS Collaboration for two years now.
- 119 Thank you to Dr. Brigitte Vachon for her guidance throughout this project and for editing
120 this thesis. I am consistently amazed by her ability to jump into the details of my project
121 and discuss them with me.
- 122 Thanks also to Dr. Benoit Lefebvre, who collected some of the data used in this thesis, wrote
123 several software tools I used to analyze the data and advised me several times throughout
124 this project.
- 125 Thank you to my labmates at McGill University, Dr. Tony Kwan, Kathrin Brunner, John
126 McGowan and Charlie Chen. Kathrin taught me mechanical skills that I will apply elsewhere.
127 Tony, manager of the laboratory, created the most encouraging, trusting and productive work
128 environment I have ever been apart of.
- 129 Thank you to the friends I can call on at anytime, and thank you to my family whose
130 constant support makes every step possible.

Contribution of authors

I, the author, was involved in collecting the cosmic ray data from September 2019 - March 2021. I did not design the cosmic ray testing procedure nor write the data preparation software, but I participated in using the software to analyze cosmic ray results. In the thesis, the terms “clustering,” “local offset” and “relative local offset” are defined. Cosmic ray clustering was done in the data preparation software, but I redid the fit afterwards to explore sensitivity to the fit algorithm. With help from Dr. Lefebvre and Dr. Vachon, I helped design the software that calculated the relative local offsets from cosmic ray data. I wrote that software on my own. I was not involved in the design, data collection, data preparation or analysis of the x-ray data. I also was not involved in creating an alignment model from the x-ray data. I used the x-ray local offsets calculated using x-ray data analysis software to calculate relative local offsets with x-rays. I did the comparison between the x-ray and cosmic ray data.

I hereby declare that I am the sole author of this thesis. This is a true copy of the thesis, including any required final revisions, as accepted by my examiners.

¹⁴⁶

Chapter 1

¹⁴⁷

Introduction

¹⁴⁸ The Standard Model (SM) is a theoretical framework that describes experimental observa-
¹⁴⁹ tions of particles and their interactions at the smallest distance scales; however, the questions
¹⁵⁰ the SM does not address motivate more experimentation.

¹⁵¹ Accelerators collide particles to generate interactions that can be recorded by detectors
¹⁵² for further study. Detectors measure the trajectory and energy of all secondary particles
¹⁵³ produced in collisions to understand the interaction. The Large Hadron Collider (LHC) [1]
¹⁵⁴ at CERN is the world’s most energetic particle accelerator. Its energy makes it a unique
¹⁵⁵ tool to study elementary particles and their interactions in an environment with conditions
¹⁵⁶ similar to what would have existed in the early universe. If study at the energy frontier is
¹⁵⁷ to continue, the LHC must go on.

¹⁵⁸ After 2025, the statistical gain in running the LHC further without significant increase in
¹⁵⁹ beam intensity will become marginal. The High Luminosity Large Hadron Collider (HL-
¹⁶⁰ LHC) project [2] is a series of upgrades to LHC infrastructure that will allow the LHC
¹⁶¹ to collect approximately ten times more data than in the initial design by \sim 2030. The
¹⁶² increase in LHC beam intensity will result in a large increase in collision rate that will make
¹⁶³ accessible and improve statistics on several measurements of interest [3], many only possible
¹⁶⁴ at the LHC and the energy frontier. The increase in beam intensity will also increase the
¹⁶⁵ level of background radiation, requiring major upgrades to the experiments used to record
¹⁶⁶ the outcomes of the particle collisions.

¹⁶⁷ The ATLAS experiment [4] is one of the LHC’s general-purpose particle detector arrays, po-
¹⁶⁸ sitioned around one of the collision points of the LHC. During the 2019-2022 Long Shutdown
¹⁶⁹ of the LHC, the most complex upgrade of the ATLAS experiment is the replacement of the
¹⁷⁰ small wheels of the muon spectrometer with the so-called New Small Wheels (NSWs) [5].

171 The detector upgrade addresses both the expected decrease in hit efficiency of the precision
172 tracking detectors and the high fake trigger rate expected in the muon spectrometer at the
173 HL-LHC. The NSWs are made of two different detector technologies: micromegas and small-
174 strip thin gap chambers (sTGCs). Micromegas are optimized for precision tracking while
175 sTGCs are optimized for rapid triggering, although each will provide complete coverage and
176 measurement redundancy over the area of the NSWs. Eight layers each of sTGCs cover the
177 NSWs. Practically, countries involved in detector constructor created quadruplet modules of
178 four sTGCs glued together that were arranged and installed over the area of the NSWs once
179 they arrived at CERN. Teams across three Canadian institutions built and characterized 1/4
180 of all the required sTGCs.

181 The sTGCs are gas ionization chambers that consist of a thin volume of gas held between two
182 cathode boards. One board is segmented into strip readout electrodes of 3.2 mm pitch. The
183 position of the particle track in the precision coordinate can be reconstructed from the strip
184 signals [5]. The sTGCs achieved the design track spatial resolution in the precision coordinate
185 of less than 100 μm per detector plane that will allow them to achieve a 1 mrad track angular
186 resolution using the 8 layers of sTGC on the NSW [6, 5]. The NSW measurement of the
187 muon track angle will be provided to the ATLAS trigger and used to reject tracks that do
188 not originate from the interaction point [5].

189 The precise measurement of a muon track angle depends on knowing the position of each
190 readout strip within the ATLAS coordinate system. To achieve this, the position of specific
191 locations on the surface of sTGC quadruplets will be monitored by the ATLAS alignment
192 system to account for time-dependent deformations [5]. Within a quadruplet module, the
193 strip positions could have been shifted off of nominal by non-conformities of the strip pattern
194 etched onto each cathode boards [7] and shifts between strip layers while gluing sTGCs into
195 quadruplets.

196 An x-ray gun was used to measure the offset of strips from their nominal position at the
197 locations that will be monitored by the ATLAS alignment system thereby providing, locally,
198 an absolute “as-built” strip position within the ATLAS coordinate system. Estimates of the
199 “as-built” positions of every readout strip are obtained by building an alignment model from
200 the available x-ray measurements [8].

201 The technique of measuring the “as-built” strip positions using x-ray data has never been
202 used before and must be validated. This thesis describes the use of cosmic muon data,
203 recorded to characterize the performance of each Canadian-made sTGC module, to validate
204 the x-ray strip position measurements. A description of how this work fits within the overall
205 alignment scheme of the NSW is also presented.

206 Chapter 2 gives a brief overview of high energy particle physics necessary to understand the
207 physics motivation of the HL-LHC and NSW upgrades. Chapters 3 and 4 present additional

208 details on the LHC, ATLAS, the NSWs, and sTGCs. In chapter [5](#), the cosmic ray testing
209 procedure and how the position of the strips can be probed with cosmics data is presented.
210 Chapter [6](#) introduces the x-ray method, and in chapter [7](#), the x-ray offsets are validated with
211 cosmic muon data. The thesis concludes with a summary and outlook in chapter [8](#).

²¹² Chapter 2

²¹³ High energy particle physics

²¹⁴ Particle physics aims to study the elementary constituents of matter. Understanding the fundamental building blocks and how they interact provides insight into how the early universe evolved to the forms of matter we observe today. This chapter introduces general concepts in particle physics relevant to understanding the physics goals of the High-Luminosity LHC (HL-LHC) and NSWs upgrade.

²¹⁹ The information on particle physics and the SM presented here is rather general; the interested reader is referred to [9, 10, 11] for more information.

²²¹ 2.1 The Standard Model

²²² The Standard Model (SM) is a theoretical framework developed in the early 1970's that describes the observed elementary particles and their interactions. It is built on a collection of quantum field theories and has been remarkably successful at predicting experimental observations, including but not limited to the existence of the top quark [12], the tau neutrino [13] and the Higgs boson [14, 15].

²²⁷ The known elementary particles described by the SM are represented in figure 2.1. There are 12 matter particles (six quarks and six leptons), 4 force-mediating particles, and the Higgs boson. Each matter particle also has an anti-matter particle pair with the same mass but opposite charge, not represented in figure 2.1. The different forces of nature are understood to be the result of the exchange of force-mediating particles between interacting (coupled) particles. Photons are mediators of the electromagnetic force, W⁺/- and Z bosons are mediators of the weak force, and gluons are mediators of the strong force. At high

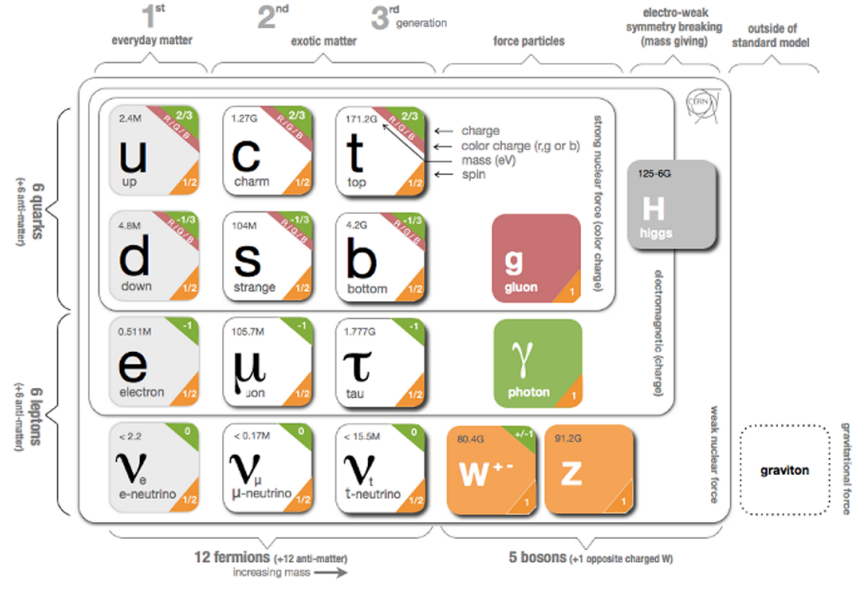


Figure 2.1: Schematic diagram of all elementary particles in the SM. Particles are grouped according to their properties and the forces through which they interact with other particles [16].

234 energy, the SM describes the electromagnetic and weak forces as stemming from a unified
 235 electroweak force. The Higgs boson field interacts with the particles mediating the unified
 236 electroweak force to distinguish the weak and electromagnetic forces from each other at lower
 237 energies and give particles (except neutrinos) a mass. This is called electroweak symmetry
 238 breaking.

239 Quarks are matter particles that are sensitive to all forces; notably they are the only particles
 240 sensitive to the strong force. Protons and neutrons are made up of quarks and gluons, and the
 241 strong force is responsible for their existence and mutual attraction into nuclei [17]. Leptons
 242 are particles not sensitive to the strong force. Charged leptons include the electron, which
 243 once part of atoms is responsible for chemistry. Of particular importance for this thesis is
 244 the charged lepton called a muon. It is like the electron but its mass is ~ 200 times larger
 245 than that of the electron. Muons have a lifetime of $2.2 \mu\text{s}$ [11] and decay predominantly as
 246 $\mu \rightarrow e^- \bar{\nu}_e \nu_\mu$. Neutrinos are neutral, almost massless leptons that only interact through the
 247 weak force.

248 Common matter is made up of the lightest constituents of the SM: up and down quarks,
249 electrons and photons. The other particles are produced in high-energy environments but
250 then decay to the lightest constituents. Such high energy environments include the condi-
251 tions present in the early universe [18], astrophysical sources, and particle accelerators. The
252 presence of the particles of the SM at the beginning of the Universe means that their inter-
253 actions and decays are fundamental for the study of the evolution of the early universe [18].
254 Many high energy astrophysical sources, like supernovae, generate particles that rain down
255 on Earth as cosmic rays [19]. Particle accelerators have been built to create controlled en-
256 vironments of high-rate, high-energy particle collisions at high energy where the production
257 and decay of elementary particles can be directly studied.

258 2.2 Beyond the Standard Model

259 Despite its success at describing most experimental observations to date, there is ample
260 evidence that the SM is not a complete description of natural phenomena at the smallest
261 scales. For example, the SM has a large number of free parameters, the values of which have
262 to be fine-tuned to fit experimental observations. This is part of the so-called “naturalness”
263 problem.

264 Furthermore, the SM provides no explanation for several open questions in particle physics.
265 First, neutrinos in the SM are assumed to be massless and do not gain mass in the same way
266 as the other particles. However, neutrino were confirmed to change between their different
267 flavours in 2013 [20], which can only occur if neutrinos do have mass [21]. The neutrino
268 mass requires physics beyond the standard model [22]. Second, several astrophysical and
269 cosmological measurements suggest the presence of “dark matter” making up 85 % of the
270 matter content of the universe [23]. The nature of dark matter is unknown and so far there
271 is no SM explanation [24]. Third, the SM does not explain the origin and nature of the
272 matter-antimatter asymmetry that produced our matter-dominated universe. Finally, the
273 SM does not include a description of gravity.

274 Theoretical extensions beyond the Standard Model (BSM) aim to address some of these
275 questions, often predicting existence of yet-unseen elementary particles or physics phenomena
276 beyond those predicted by the SM. These hypothetical new physics phenomena or new
277 particles can be searched for at particle accelerators.

278 **2.3 Studying high energy particle physics with accelerators**

279

- 280 In particular, particle accelerators of increasingly higher energy have a long history of enabling the discovery of predicted particles. These include, for example, the discovery of the W [25, 26] and Z bosons [27, 28], the top quark [29, 30], and most recently, the Higgs boson [31, 32]. The discovery of the Higgs boson marked the completion of the SM as it is known today.
- 285 Based on the established success of the SM, there are two approaches to particle physics research. One approach is to search for the existence of new physics phenomena predicted to exist in BSM theories and the other is to test the validity of the SM to a high degree of accuracy to search for flaws in the model. Standard Model predictions are generally expressed in terms of the probability of a specific physics process to occur, expressed as a cross section in units of barns (with 1 barn = 10^{-28} m²). As an example, figure 2.1 shows a summary of cross section measured for different physics processes using the ATLAS experiment and their comparison with the predictions of the SM. Most cross section measurements agree well within one standard deviation with the SM predictions.
- 294 Particle accelerators provide a controlled and high-collision rate environment that makes them ideal places to search for new physics phenomena and to carry out systematic tests of the SM. The LHC is the highest energy collider in the world so it can access physics that no other accelerator can. A description of the LHC and the ATLAS detector are provided in the next chapter.

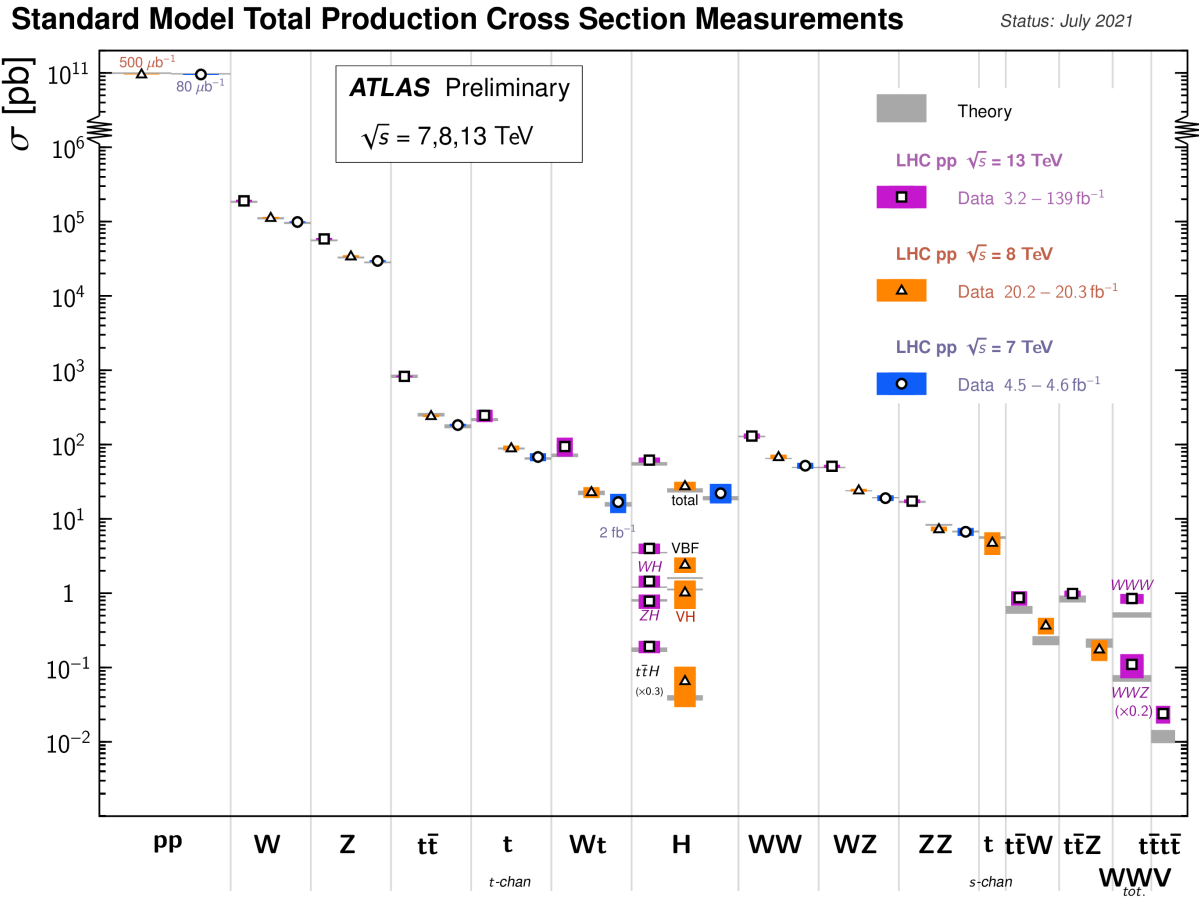


Figure 2.2: Production cross sections of different final states measured by the ATLAS experiment at the LHC. Comparison with the SM theory predictions is also shown [33].

299 **Chapter 3**

300 **The LHC and the ATLAS experiment**

301 The Large Hadron Collider (LHC) is the world’s most energetic particle accelerator and the
302 ATLAS experiment is used to record the results of particle collisions at the LHC. In this
303 chapter, details about both that are necessary to understand the High-Luminosity LHC (HL-
304 LHC) upgrade project and the ATLAS experiment’s New Small Wheels (NSWs) upgrade
305 are presented.

306 **3.1 The Large Hadron Collider**

307 The LHC is an accelerator 27 km in circumference and located \sim 100 m underground at
308 the CERN laboratory near Geneva, Switzerland [1]. It has two beam pipes within which
309 bunches of protons counter-circulate before being collided in the center of one of four major
310 experiments, such as the ATLAS experiment (discussed in section 3.3). Protons are guided on
311 the circular trajectory using 1232 superconducting dipole magnets capable of a maximum
312 field of 8.33 T. Radio-frequency accelerating cavities are used to accelerate protons to a
313 the maximum design energy of 7 TeV [34]. During LHC Run-1 (2011-2012), protons were
314 collided at a collision center-of-mass energy of 7 TeV and 8 TeV [35]. During LHC Run-2
315 (2015-2018), the center-of-mass energy of proton collisions was increased to 13 TeV [36],
316 close to the maximum design value of 14 TeV [34]. It is not actually the protons that
317 interact, but the constituent quarks and gluons that each carry some fraction of the energy
318 and momentum of the collisions.

319 **Luminosity**

320 The number of proton-proton interactions generated by the LHC directly affects the statistics

available to make measurements of interaction cross sections. Predicting the number of proton-proton interactions requires defining a metric called luminosity [11]. The luminosity of a particle collider is the number of particles an accelerator can send through a given area per unit time. It is calculated from the measurable quantities in Equation 3.1:

$$\mathcal{L} = \frac{f N_1 N_2}{4\pi\sigma_x\sigma_y}, \quad (3.1)$$

where f is the frequency of the bunch crossings (25 ns), N_1 and N_2 are the number of protons in each bunch ($\sim 10^{11}$ protons / bunch), and σ_x and σ_y are the RMS of the spatial distributions of the bunch. Therefore, luminosity is a property of accelerator beams, which are set by the capabilities of the accelerator. The design luminosity of the LHC was $10^{34} \text{ cm}^{-2}\text{s}^{-1}$. The units of luminosity are an inverse area; multiplying the luminosity by the cross section of a given process gives the expected rate for that process.

Integrating the *instantaneous* luminosity (equation 3.1) over a period of data collection time gives the integrated luminosity,

$$L = \int \mathcal{L}(t) dt \quad (3.2)$$

which is related to the total number of interactions. In this way, the luminosity is the link between the accelerator and the statistical power of measurements to be made with the data collected. So far, the LHC provided an integrated luminosity of 28.26 fb^{-1} in Run-1 [35] and 156 fb^{-1} in Run-2 [36].

3.2 The High-Luminosity LHC

At the end of the LHC program in 2025, the statistical gain on measurements in running the LHC further will become marginal. The HL-LHC [2] project consists of the upgrade of LHC infrastructure to achieve a nearly ten fold increase in instantaneous luminosity, thereby improving measurement statistics as well. Also, some systems will need repair and replacement to operate past ~ 2020 . The LHC will continue to be the most energetic accelerator in the world for years to come and is the only accelerator with enough energy to directly produce the Higgs boson and top quarks. Therefore, the European Strategy for Particle Physics made it a priority “to fully exploit the physics potential of the LHC” with “a major luminosity upgrade” [37]. The goal is for the HL-LHC to provide an integrated luminosity of 3000 fb^{-1} in the 12 years following the upgrade. The luminosity actually



Figure 3.1: The LHC/HL-LHC timeline [38]. The integrated luminosities collected and projected for each run of the LHC are shown in blue boxes below the timeline and the center of mass energy of the collisions is shown in red above the timeline. The top blue arrow labels the run number. The acronym “LS” stands for “long shutdown” and indicates periods where the accelerator is not operating. During the shutdowns, upgrades to the LHC and the experiments are taking place. This timeline was last updated in January, 2021, and reflects changes in the schedule due to the ongoing pandemic.

348 achieved will depend on a combination of technological advances and upgrades in progress
 349 that affect the factors contributing to luminosity defined in equation 3.1 [2]. Figure 3.1 shows
 350 the projected schedule of the HL-LHC upgrades and operation [38].

351 One of the most anticipated measurements at the HL-LHC is the value of the triple-Higgs
 352 coupling. Measuring the coupling will allow the determination of the shape of the Higgs
 353 potential responsible for electroweak symmetry breaking. Any discrepancy with respect to
 354 the SM prediction will show that there must be other sources of electroweak symmetry
 355 breaking, and hence physics phenomena beyond the SM. The LHC is the only accelerator
 356 where the Higgs boson can be produced directly so it is the only place where the triple-Higgs
 357 coupling could be measured. The HL-LHC upgrade is required to produce a significant
 358 sample of Higgs produced in pairs to make a statistically meaningful measurement [3, 39].

359 Accordingly, detector sensitivity to various Higgs decays will be important at the HL-LHC.

360 3.3 The ATLAS experiment

361 The ATLAS experiment [4] was designed to support all the physics goals of the LHC. It
362 is 44 m long and 25 m in diameter, and weighs 7000 tonnes. The ATLAS experiment is
363 centered around one of the LHC's interaction points (a place where the beams collide). As
364 shown schematically in figure 3.2, ATLAS consists of an array of particle detector subsystems
365 arranged concentrically around the beam pipe. The ATLAS experiment is cylindrical because
366 it aims to provide 4π coverage around the interaction point. In reference to the cylindrical
367 geometry of the experiment, it is helpful to separate the subsystems of ATLAS into the
368 so-called "barrel" and "endcap"/"forward" regions.

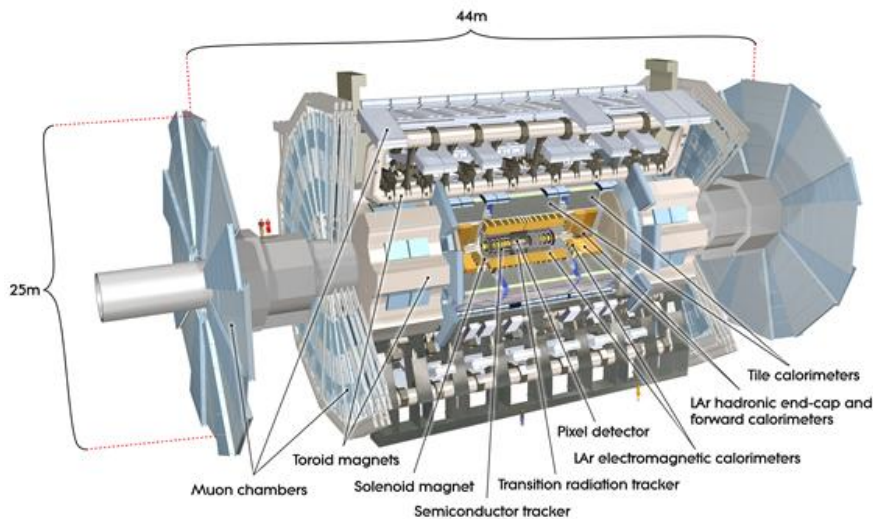


Figure 3.2: Schematic diagram of the ATLAS experiment, with the various detector subsystems labelled [4].

369 For analysis purposes, a spherical coordinate system is defined. The azimuthal angle ϕ is
370 measured around the beampipe and the polar angle θ is measured from the beam pipe. The
371 polar angle is more often expressed in terms of pseudo-rapidity, defined as $\eta = -\ln \tan(\theta/2)$.
372 Pseudo-rapidity values vary from 0 (perpendicular to the beam) to $\pm\infty$ (parallel to the
373 beam, defined as the z-direction) and is an approximation to the rapidity of a particle when
374 its momentum is much greater than its mass. It is useful to describe the direction of outgoing

375 particles in proton-proton collisions because differences in rapidity are invariant to a Lorentz
376 boost along the beam direction.

377 The ATLAS experiment provides identification and kinematic measurements for each particle
378 created after the initial collision, which is done by assembling offline the information recorded
379 by each subsystem. With this information, signatures of processes of interest can be identified
380 and studied. An overview of the main ATLAS subsystems is given below.

381 **The inner detector**

382 The inner detector [40, 41] (figure 3.3) is for precise measurements of charged particle tra-
383 jectories, measurement of primary and secondary interaction vertices and assistance in the
384 identification of electrons. A 2 T solenoid with field parallel to the beam bends the trajec-
385 tory of outgoing charged particles. A measurement of the bending radius of each charged
386 particle provides information about its momentum. The innermost part of the inner tracker
387 is made of high-resolution semiconductor pixel and strip detectors while the outermost part
388 is made of straw-tubes. The straw tubes are used in the trajectory measurements but they
389 are also interspersed with material designed to enhance the creation of transition radiation.
390 Transition radiation occurs when a highly relativistic charged particle traverses a material
391 boundary [42]. The amount of transition radiation emitted by a charged particle is detected
392 by the straw-tubes and is used to identify electrons.

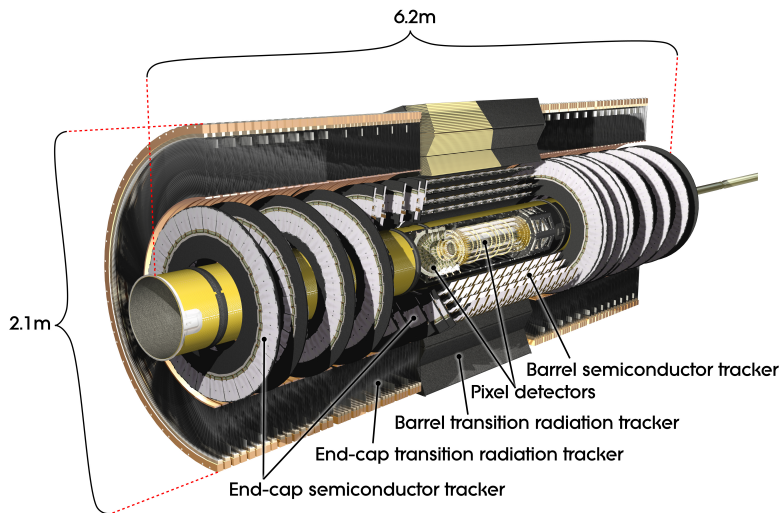


Figure 3.3: Schematic diagram of the ATLAS experiment's inner detector, with the different segments and the technology used labeled [4].

393 **Calorimetry system**

394 Electromagnetic and hadronic sampling calorimeter units are used to record the energy
395 of electrons, photons and jets¹. A combination of liquid-argon (LAr) electromagnetic and
396 hadronic calorimeters [43] and tile-scintillator hadronic calorimeters [44] cover the rapidity
397 range $|\eta| < 4.9$, as shown in figure 3.4.

398 Sampling calorimeters have alternating layers of dense material and material that can mea-
399 sure the amount of ionization by charged particles. The dense material causes incoming
400 charged particles to shower into lower energy particles and deposit their energy in the sen-
401 sitive volume. Only muons and neutrinos are known to pass the calorimeters to the muon
402 spectrometer without being absorbed.

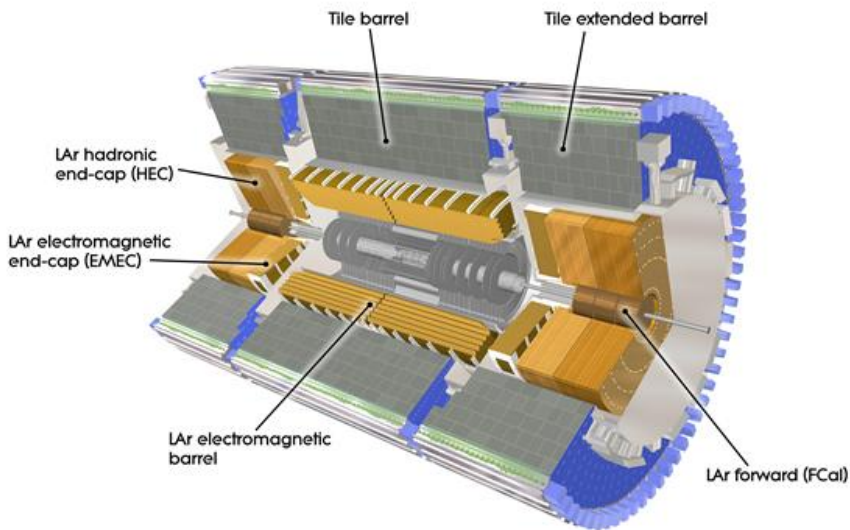


Figure 3.4: Schematic diagram of the ATLAS calorimeter system, with the different segments and the technology used labeled [4].

403 **Muon spectrometer**

404 The muon spectrometer [45] consists of multiple layers of tracking chambers embedded in
405 a 2 T magnetic field generated by an air-core superconducting toroid magnet system. Fig-
406 ure 3.5a shows a schematic diagram of the layout of the different chambers and of the toroid

¹When quarks or gluons are expelled in a high energy collision, they create collimated groups of hadrons called jets because they carry a charge called “colour”, and nature only allows “colourless” combinations to exist [42].

407 magnets [4]. The trajectory of a muon is reconstructed from the information recorded by
 408 the different types and layers of tracking chambers. The amount of bending in the magnetic
 409 field provides a measure of the muon's momentum. In the barrel section of ATLAS, the
 410 toroidal magnetic field is created by eight coils bent into the shape of a "race-track" and
 411 symmetrically arranged around the beampipe. In the forward region, two end-cap toroids,
 412 each with eight smaller racetrack-shaped coils arranged symmetrically around the beam pipe
 413 are inserted in the ends of the barrel toroid [46].

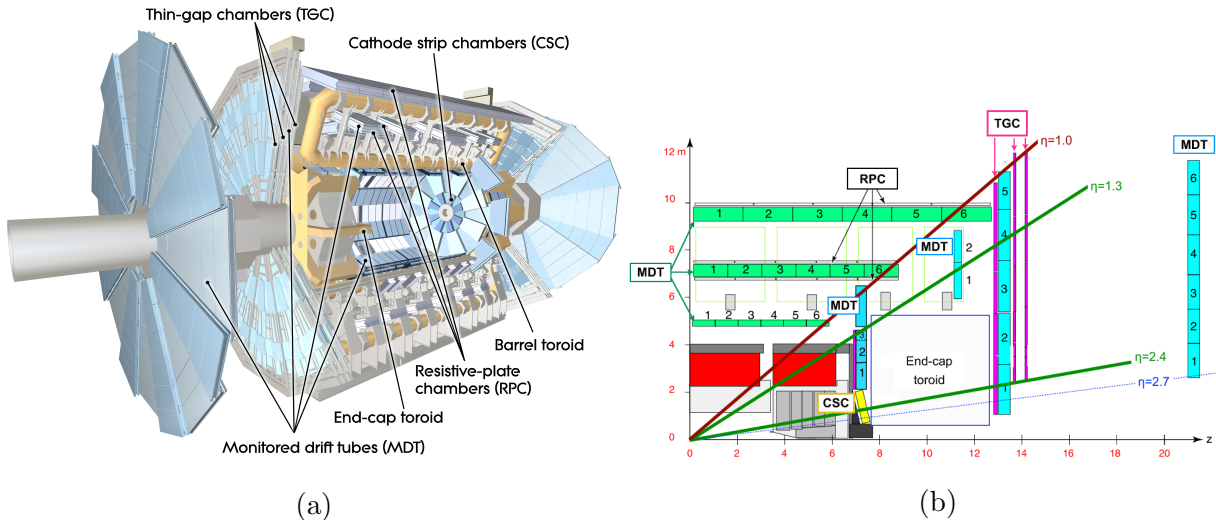


Figure 3.5: Schematic diagram of the ATLAS muon spectrometer. Figure (a) shows a 3D projection of the system with the different types of chambers and different parts of the toroidal magnet system labeled [4]. Figure (b) shows a projection of one quarter of the muon spectrometer, with the interaction point in the bottom left corner. The small wheel is just left of the end cap toroid, the big wheel is to its right, and the outer wheel is the rightmost structure [47].

414 The muon spectrometer is separated into detectors used for precision offline tracking and
 415 for triggering purposes. Three layers of monitored drift tubes (MDTs) or cathode strip
 416 chambers (CSCs) are used for tracking. The position of the muon track in each of the three
 417 layers allows reconstruction of the bent trajectory of a muon and hence its momentum. To
 418 satisfy the muon spectrometer target momentum resolution of $\Delta p_T/p_T < 1 \times 10^{-4} p / \text{GeV}$
 419 for $p_T < 300 \text{ GeV}$ and a few percent for lower p_T muons, the MDTs and CSCs were designed
 420 to achieve a spatial resolution of $50 \mu\text{m}$ each. Accordingly, an optical alignment system was
 421 designed to monitor and correct for chamber positions [45, 48].

422 Resistive plate chambers (RPCs) are used for triggering in the barrel and thin-gap chambers

423 (TGCs) are used for triggering in the endcaps. The positions of each type of chamber
424 are sketched in figure 3.5b. The endcap section of the muon spectrometer consists of three
425 sections, the small wheel, big wheel, and outer wheel – ordered by proximity to the interaction
426 point. In Run-1, low (high) p_T muons were triggered on if two (three) of the RPC or TGC
427 layers around the big wheel fired in coincidence, for the barrel and endcaps respectively [49].
428 After Run-1 it was discovered that up to 90% of the triggers in the endcap were fake, caused
429 by background particles generated in the material between the small wheel and the big
430 wheel [5]. To reduce the fake rate in Run-2, the TGCs on the inside of the small wheel also
431 had to register a hit. The added condition reduced the trigger rate by 50% in the range $1.3 < |\eta| < 1.9$ [50]. The effectiveness of the solution was limited since the $|\eta|$ -range of the small
433 wheel TGCs was limited to $1.0 < |\eta| < 1.9$ and the spatial resolution of the small wheel
434 TGCs is coarse [5].

435 Trigger system

436 It would be impossible to record all the data from bunch crossings every 25 ns, corresponding
437 to a rate of ~ 40 MHz. The ATLAS experiment has a multi-level trigger system to select
438 events of interest for permanent storage. The Level-1 (L1) hardware trigger [49] uses partial-
439 granularity information from the muon spectrometer and calorimeters to trigger on high p_T
440 muons, electrons, jets, missing transverse energy, and τ decaying to hadrons. After Run-3
441 an upgrade of the trigger system will allow a maximum trigger rate of 1 MHz with a latency
442 of 10 μ s [51], but for now the working limits are a rate of 100 kHz [50] and 2.5 μ s [49].

443 The L1 trigger is used to define regions of interest that are fed into the software high level
444 trigger (HLT) [52], in which the full granularity of the muon spectrometer and calorimeter
445 are used with information from the inner detector to reduce the trigger rate to 1 kHz. Events
446 that satisfy at least one of the L1 and HLT trigger criteria are recorded to permanent storage
447 for offline analysis.

448

449 With the foreseen increase in luminosity at HL-LHC, it is a priority to upgrade the ATLAS
450 detector to further reduce the muon trigger fake rate in the forward region. The New Small
451 Wheels being commissioned to replace the original ATLAS muon small wheels will address
452 this challenge.

453 **Chapter 4**

454 **The New Small Wheels**

455 **4.1 Motivation for the New Small Wheels**

456 The hit rate of all detector systems will significantly increase during HL-LHC operation
457 because of the increase in luminosity. The increased rate presents a challenge for both the
458 tracking and triggering capabilities of the muon spectrometer [5].

459 In terms of precision tracking, the maximum hit rate in the MDTs is expected to reach above
460 300 kHz by the end LHC operation. At this rate, the hit efficiency of MDTs decreases by
461 35%, mostly due to the long dead-time of the chambers. Losing hits in the small wheel will
462 reduce the high p_T muon momentum resolution. The decrease in resolution will affect the
463 ability to search for, for example, the decay of hypothetical heavy bosons (W' , Z') or other
464 hypothetical particles beyond the SM [3].

465 Already during LHC Run-2 operation, the forward muon trigger system had to cope with a
466 very high fake rate, even with the inclusion of TGC data from the small wheel as part of the
467 trigger criteria. At the luminosity expected in Run-3, it is estimated that 60 kHz out of the
468 maximum L1 trigger bandwidth of 100 kHz would be taken up by forward muon triggers.
469 To address this challenge, a possible solution would be to raise the minimum p_T threshold
470 from 20 GeV to 40 GeV. However, this would have an adverse impact on the ability to study
471 several physics processes of interest that depend on low p_T muons, particularly the Higgs
472 decay to two muons, the Higgs decay to two tau leptons and hypothetical particle decays
473 beyond the SM [5].

474 The NSWs will address both of these problems. They will be made of precision tracking
475 chambers suitable for the expected hit rates during the HL-LHC and triggering chambers
476 capable of 1 mrad track angular resolution. The idea behind the design triggering capability

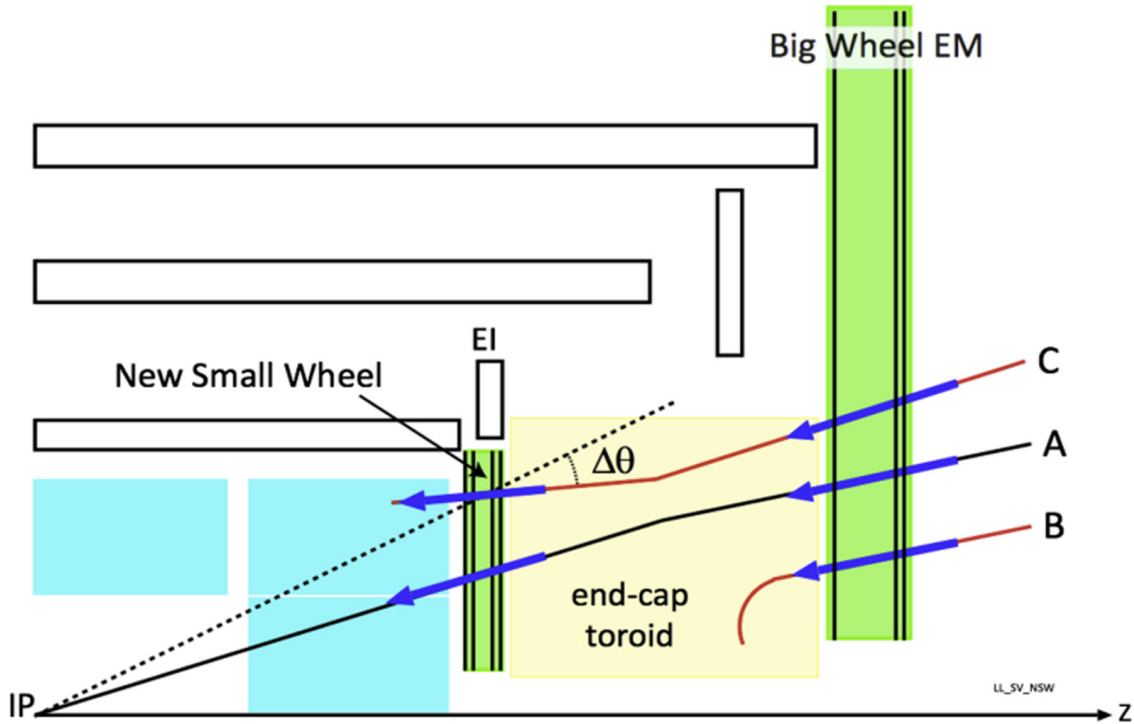


Figure 4.1: A schematic diagram of a quarter cross section of the ATLAS muon spectrometer, with the interaction point (IP) in the bottom left corner. Three possible tracks are labeled. Ideally, track A would be triggered on while track B and C discarded. With the old small wheel, all three tracks would be recorded. With the NSW, only track A would be recorded [5].

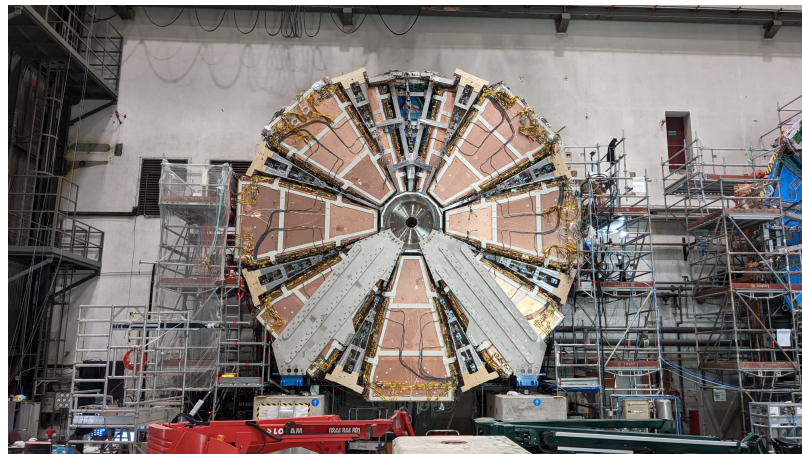
477 of the chambers is to allow matching of track segments measured by the NSW with track
 478 segments from the big wheel to discard tracks not originating from the interaction point.
 479 Figure 4.1 illustrates this point: the Run-2 trigger system would have triggered on all three
 480 tracks (A, B, C) while with the NSW the trigger system would only trigger on track A.
 481 The NSWs will therefore make it possible to maintain a low muon p_T trigger threshold and
 482 maintain an adequate muon momentum resolution during HL-LHC operations, which will
 483 allow the full exploitation of the physics potential of this research program [5].



(a) A sTGC quadruplet module. The left image highlights the trapezoidal shape of a quadruplet module. The right image shows the corner at the short edge, where the four sTGC layers and each layer's gas inlet are visible. The gas outlets and high voltage cables are located along the long edge near the corner in the back left of the photo. The green printed circuit board along the sides are the adaptor boards where the front end electronics are attached.



(b) Left: A sTGC wedge. The white frame outlines the individual quadruplet modules that have been glued together into a wedge. Right: A completed sector, with two sTGC wedges on the outside and two micromegas wedges on the inside.



(c) A picture of one of the two NSWs. All sectors except one large sector at the top are installed, revealing two of the smaller sectors that are normally hidden under the large sectors and support bars. The NSWs are 9.3 m in diameter.

Figure 4.2: Images showing different stages of NSW construction.

484 **4.2 Design of the NSWs**

485 The NSWs are made with two detector technologies: micromegas and small-strip thin gap
486 chambers. Eight layers of each cover the entire area of the wheel. Micromegas are designed
487 to be the primary precision tracking detectors and sTGCs the primary triggering detectors,
488 but both technologies offer full redundancy by being capable of providing both precision
489 measurements and trigger information. Both types of detectors were designed to achieve
490 spatial resolution better than $\sim 100 \mu\text{m}$ per layer. Four chambers are glued together to create
491 quadruplet modules of each detector type. Quadruplets of different sizes, most shaped as
492 trapezoids, are assembled into wedges. Two sTGC wedges and two micromegas wedges are
493 layered to create sectors (with the sTGC wedges on the outside) [5]. Different stages of the
494 construction process are shown in figure 4.2. At the time of writing, the assembly of the
495 NSWs has just been completed. The first NSW has been lowered into the ATLAS cavern
496 and is being commissioned and the second will be lowered shortly.

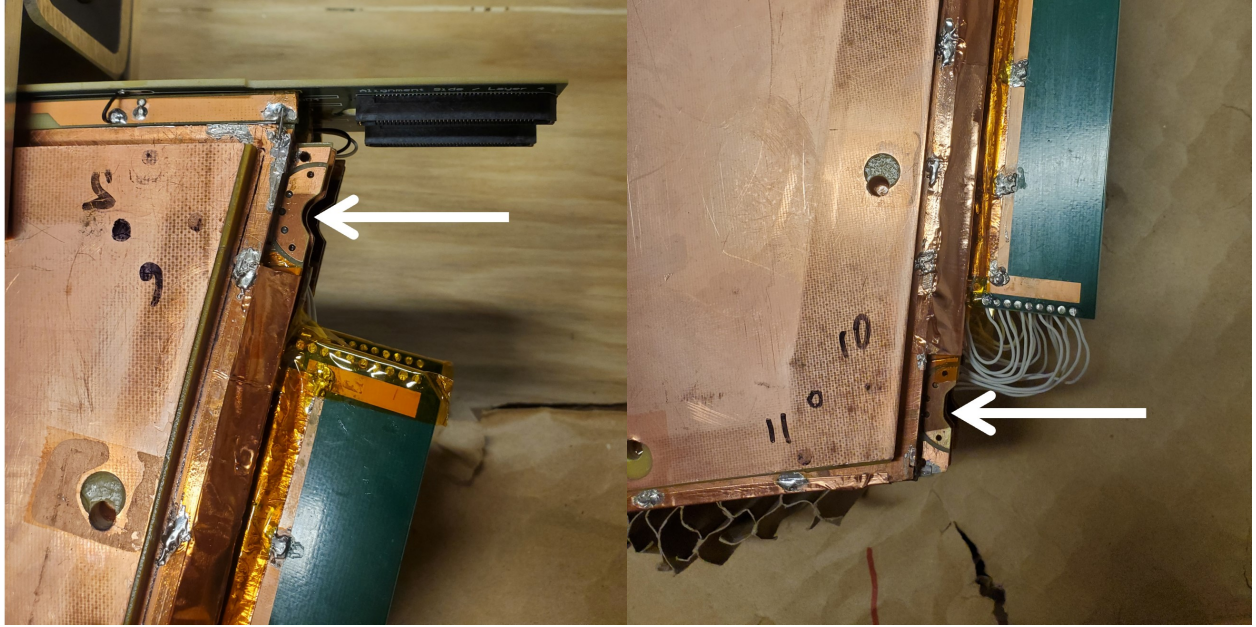
497 **4.3 Small-strip thin gap chambers**

498 The sTGCs are gas ionization chambers operated with a gas mixture of CO₂:n-pentane with
499 a ratio of 55%:45% by volume. Gold-plated tungsten wires, 50 μm in diameter and with
500 1.8 mm pitch, are suspended between two cathode planes made of FR-4, each 1.4 mm away
501 (see figure 4.3). One cathode board is segmented into copper pads of varying area (with a
502 typical size of $\sim 300 \text{ cm}^2$ each), and the other is segmented into copper strips of 3.2 mm pitch
503 running lengthwise perpendicular to the wires. High voltage is applied to the wires and the
504 cathode planes are grounded [5, 53]. When a muon passes through a sTGC, it will ionize some
505 of the atoms in the gas and the electric field in the gas gap will result in the formation of an
506 ionization avalanche [54]. The motion of the ions and free electrons generates small currents
507 on the nearby wire and capacitatively-coupled strip and pad electrodes [5]. The gas mixture
508 was chosen to absorb excess photons produced in the avalanche that delocalize the avalanche
509 signal [55] and saturate many strip electrodes, preventing the formation of streamers [42].
510 This allows the chambers to be run at a higher high-voltage providing a faster response and
511 higher signal [55]. The resistivity of the carbon coating and capacitance of the pre-preg
512 sheet tune the spread of the charge distribution [56] and the speed of the response [57] to
513 optimize the rate capability. The combined information from the strip readout electrodes
514 and wires provide the location where the muon passed through the chamber. The small pitch
515 of the strip readout electrodes is what allows the quadruplets to deliver good track angular
516 resolution to improve the fake trigger rate and meet the precision tracking requirements [5].



Figure 4.3: Internal structure of an sTGC, zoomed into the area under a pad. High voltage is applied to wires suspended in the gas volume to create an electric field. A passing muon causes an ionization avalanche that is picked up by the wire, strip and pad electrodes [8].

- 517 A 3-out-of-4 coincidence in pad electrodes from each layer of a quadruplet defines a region of
 518 interest where the strip and wire electrodes should be read out. The pad triggering scheme
 519 greatly reduces the number of electrodes that require readout so that a track segment of the
 520 required angular resolution can be provided quickly enough to the hardware trigger [5].
- 521 Signal is read out from groups of successive wires, so the position resolution in the direction
 522 perpendicular to the wires is 10 mm per plane. The wires give the azimuthal coordinate
 523 in ATLAS so the position resolution in this direction is sufficient. Good resolution on the
 524 η coordinate, perpendicular to the strips, is important [5]. In a test beam environment,
 525 the strip spatial resolution of a single sTGC was measured to be 45 microns for muon
 526 perpendicularly incident on the surface of the sTGC. Although the spatial resolution worsens
 527 as function of muon angle measured from normal incidence [58], when four sTGCs are glued
 528 together into a quadruplet the design angular resolution of 1 mrad in the strip coordinate is



(a) Brass insert near long edge.

(b) Brass insert near short edge.

Figure 4.4: The brass inserts sticking out from the gas volumes of an sTGC quadruplet. These inserts were pressed against alignment pins when the individual sTGCs were being glued together.

529 achievable [5, 53].

530 To achieve the required track angular resolution once installed in ATLAS, the absolute
 531 position of each sTGC strip within the ATLAS coordinate system must be accurately known.
 532 The degree of accuracy required is on the order of the position resolution of the chambers,
 533 $\sim 100 \mu\text{m}$. The NSW alignment system, detailed in section 4.5, will monitor the position of
 534 alignment platforms installed on the surface of the wedges. The alignment platforms are
 535 installed with respect to an external reference on the sTGCs: two brass inserts on each strip
 536 layer on one of the angled sides of each quadruplet (shown in figure 4.4). So the challenge
 537 of monitoring the position of the strips in ATLAS was separated into two steps: first, infer
 538 the position of the strips with respect to the brass inserts using the sTGC design geometry;
 539 second, use the alignment system to monitor the position of the alignment platforms. The
 540 next section provides some pertinent details on the sTGC construction process, with steps
 541 that affect the position of the strips with respect to the brass inserts highlighted.

542 4.4 sTGC Quadruplet Construction

543 Five countries were responsible for producing sTGC quadruplets of varying geometries for the
544 NSW: Canada, Chile, China, Israel and Russia. Canada was responsible for the construction
545 of one quarter of the required sTGCs, of three different quadruplet geometries. The steps of
546 the construction process in each country were similar [5]. The process followed in Canada is
547 detailed here.

548 A research group at TRIUMF in Vancouver, British Columbia was responsible for preparing
549 the cathode boards. The boards were made and the electrodes etched on at a commercial
550 laboratory, Triangle Labs, in Carson City, Nevada. Once completed they were sent to TRI-
551 UMF to be sprayed with graphite and to have support structures glued on [7]. The boards
552 are commercial multilayer printed circuit boards, but the strip boards required precision ma-
553 chining to etch the strip pattern [5]. Triangle Labs also machined the two brass inserts into
554 each strip board. A coordinate measuring machine (CMM) was used to accurately measure
555 the position of a set of reference strips on each board. Four quality parameters describing
556 non-conformities in the strip pattern of each board with respect to the brass inserts were
557 derived from the data and the results are available on a QA/QC database. The parameters –
558 offset, angle, scale and nonparallelism – and the CMM data collection is described in full
559 in [7]. Due to time constraints, tolerances on the non-conformities in the etched strip pattern
560 with respect to the brass inserts were loosened, with the condition that the strip positions
561 in ATLAS would have to be corrected for [7].

562 The prepared boards were sent to Carleton University in Ottawa, Ontario for construction
563 into sTGCs and quadruplets. First, the wires were wound around the pad cathode boards
564 using a rotating table and the wires were soldered into place. A wound pad cathode board glued
565 was held by vacuum on a granite table, flat to within 20 μm , and a strip cathode board glued
566 on top to create an sTGC. Holding one sTGC flat with the vacuum, another was glued on
567 top to create a doublet, then two doublets were glued together to create a quadruplet. When
568 gluing sTGCs together, the brass inserts were pushed against alignment pins with the goal of
569 keeping the strip layers aligned within tolerance. However, non-conformities in the shape of
570 the brass inserts, non-conformities in the position of the alignment pins and shifts between
571 sTGCs while the glue cured resulted in misalignments between the brass inserts and strip
572 layers. Precise alignment of the pad boards or wires with respect to the strip boards did
573 not have to be so tightly controlled because pads and wires do not measure the precision
574 coordinate.

575 The Carleton team finished the quadruplets by installing adaptor boards on the angled sides
576 of each layer that allow front end electronics to be attached. Completed quadruplets were
577 sent to McGill University where their performance was characterized with cosmic rays. De-

578 tails pertaining to cosmic ray testing of sTGC quadruplets at McGill University are described
579 in chapter 5. Tested quadruplets were sent to CERN where they were assembled into wedges
580 and alignment platforms installed. The alignment platforms were installed using a jig posi-
581 tioned with respect to the brass inserts. Completed wedges were assembled into sectors then
582 installed on the NSWs.

583 The quadruplet construction process had two steps where strip positions could be shifted off
584 of nominal. At board-level, there could be non-conformities in the etched strip pattern with
585 respect to the brass inserts, described by the four quality parameters [7]. At the quadruplet
586 level, misalignments between the brass inserts and strips on different layers were possibly
587 introduced during the gluing. The result was that the brass inserts were not a reliable
588 reference point and that the strips can be offset from their design position by up to hundreds
589 of micrometers. Offsets in strip positions from nominal in Canadian quadruplets were shown
590 to be random [7], so no one correction would suffice. The offsets must be measured and
591 corrected for in the ATLAS offline software that does the precision tracking. Understanding
592 the work ongoing to make measurements of strip position offsets and correct for them requires
593 understanding the strategy of the NSW alignment system.

594 4.5 NSW alignment

595 The idea of the NSW alignment system is presented in [5], but the details have only been
596 presented internally so far. After the wedges are constructed, alignment platforms are in-
597 stalled on every sTGC quadruplet and optical fibres routed to them, as shown in figure 4.5.
598 Light from the optical fibres will be monitored in real time by cameras (BCAMs) mounted on
599 the alignment bars of the NSWs. The system will thus record the positions of the alignment
600 platforms in the ATLAS coordinate system and any changes over time.

601 The original alignment scheme was to use the brass inserts as a reference between the align-
602 ment platforms and the individual strips, as shown in the solid arrows in figure 4.6 – this
603 will no longer work. The position of the alignment platforms will be known thanks to the
604 alignment system, so a different method to get the position of the strips with respect to the
605 alignment platforms is currently in its final stage of development. The technique consists of
606 the measurement of the strip pattern offset at a few areas on the surface of a sTGC quadru-
607 plet using an xray gun mounted on the alignment platforms. The local strip pattern offset
608 with respect to nominal geometry at the location of each alignment platform is obtained
609 by analyzing the xray gun beam profile. As shown in figure 4.6, this approach essentially
610 bypasses the need to know the position of strips with respect to the brass inserts. The align-
611 ment platforms provide the link to the nominal geometry because the nominal group of strips

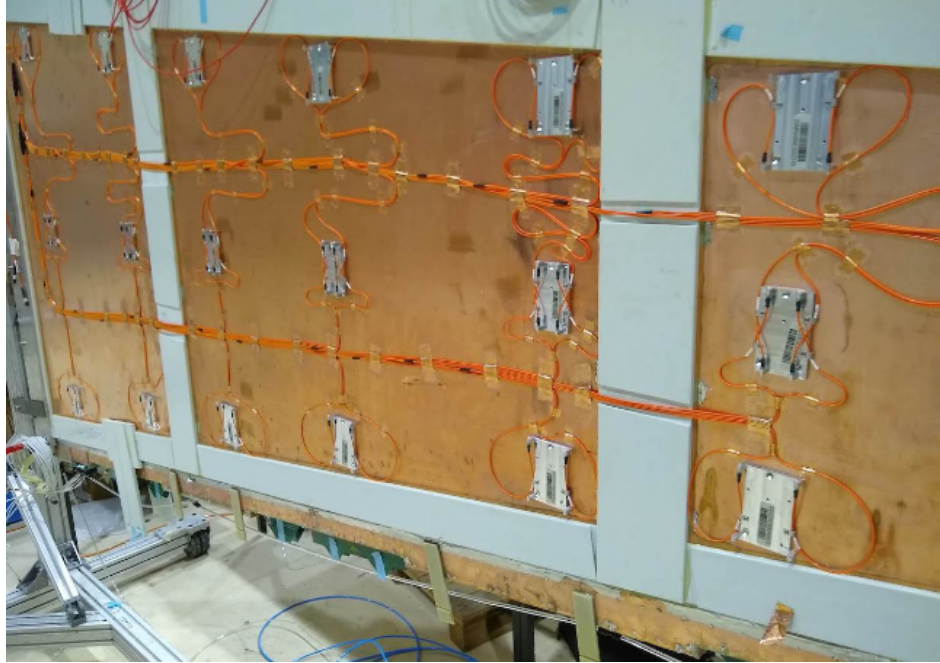


Figure 4.5: A sTGC wedge with alignment platforms (silver) installed on the quadruplet. Optical fibres (orange) are routed to the alignment platforms. Cameras on the frames of the NSWs will record light from the optical fibres to monitor in real-time the position the alignment platforms in the ATLAS coordinate system.

612 that should be nearest to them can be identified using the nominal geometry parameters that
 613 assume the strips are perfectly etched and aligned. Cosmic muon track positions cannot be
 614 compared to the nominal geometry because the alignment platforms are not installed when
 615 cosmics data is collected, so there is no external reference to provide a link to the nominal
 616 geometry.

617 The x-ray method does not have the sensitivity to measure the offset of each strip from
 618 nominal, but what can be measured instead is the offset of the strip pattern in a local area
 619 around the position of the gun. *Local offsets* are used to build an alignment model for each
 620 strip layer. Formally defined, an alignment model is a set of parameters used to estimate the
 621 “as-built” position of a strip given its nominal position. The alignment model currently being
 622 worked on takes x-ray and CMM data as input to calculate an overall offset and rotation of
 623 each strip layer with respect to nominal [8]. The alignment parameters could be described
 624 as “global”, meaning over the whole layer instead of local. Without the x-ray dataset, there
 625 would be no input to the alignment model that takes into account inter-layer misalignments
 626 introduced during quadruplet construction.

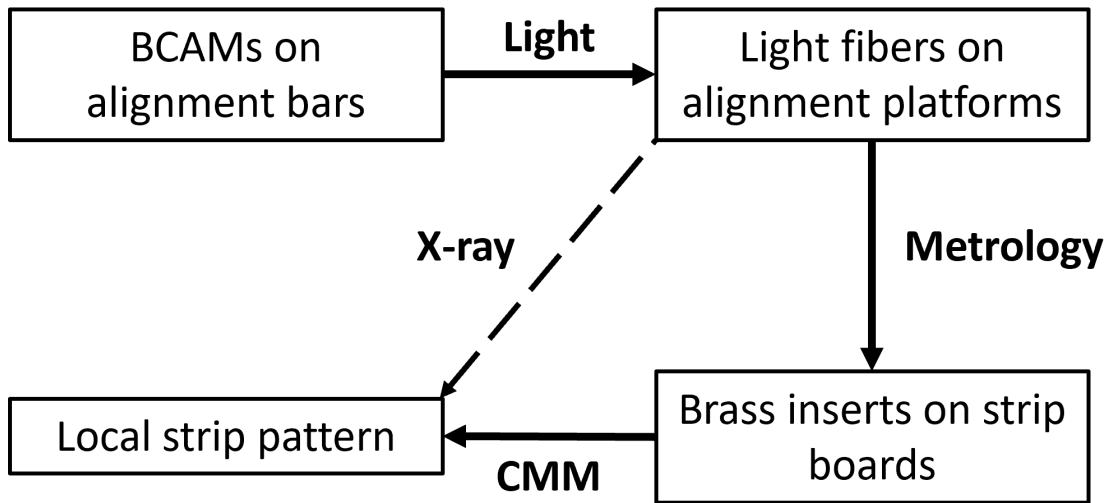


Figure 4.6: Schematic diagram showing how the different elements of the sTGC alignment system relate to one another. The solid arrows denote the planned alignment scheme. The dashed arrow shows the modification being finalized now. This figure was originally designed by Dr. Benoit Lefebvre.

Given that the x-ray local offsets can only be measured at positions where the gun can be attached and that they are an important part of the alignment scheme, the new x-ray measurement technique needs to be validated. The goal of this thesis is to validate the x-ray local offsets while exploring how cosmics data complements and adds to the understanding of strip positions and global alignment.

632 Chapter 5

633 Using cosmic muons to measure 634 relative strip position offsets

635 At McGill University, among other quality and functionality tests, each Canadian-made
636 quadruplet was characterized with cosmic muons. In this chapter, the experimental setup and
637 how the data was analyzed to provide relative strip position offsets is presented. The analysis
638 method was motivated by the how the measurements could be compared to measurements
639 done with the x-ray method (chapter 6) but also it stands alone as a characterization of the
640 alignment between strips of different layers. The chapter begins with a brief introduction to
641 cosmic rays.

642 5.1 Cosmic rays

643 The earth is being constantly bombarded by particles from the sun, galactic sources and
644 extra galactic sources – collectively called cosmic rays [19, 11]. Cosmic rays consist mostly
645 of protons, but also heavier ions, gamma rays and the term sometimes includes neutrinos.
646 The primary (initial) cosmic ray interacting with the atmosphere causes electromagnetic and
647 hadronic showers of secondary particles. Hadronic showers result from the primary cosmic ray
648 interacting strongly with the target of the atmosphere, resulting in an abundant production
649 of pions. Charged pions predominantly decay to muons (there is a lesser contribution to
650 the muon flux from kaons as well) [59]. The secondary muons are relativistic and thanks
651 to time dilation their lifetime is extended as measured in the reference frame of earth, so a
652 flux of approximately 1 muon/cm²/ min reaches the ground [11]. Measuring the muon flux
653 and energy spectrum reveals information about primary cosmic rays [59] which is interesting

654 to high energy physicists and astrophysicists. The muon flux is also terribly convenient for
655 testing muon detectors.

656 **5.2 Experimental setup**



Figure 5.1: Cosmic muon hodoscope at McGill University with a sTGC quadruplet module in the test bench.

657 Cosmic muon characterization of sTGC quadruplet modules was done with a hodoscope, a
658 complete description of which can be found in [58]. The quadruplet was placed in the center
659 of the test bench. Above and below it was a layer of scintillator-PMT arrays, as shown in
660 figure 5.1. When a cosmic muon passed within the acceptance of the hodoscope, at least one
661 scintillator from the top array and at least one from the bottom array fired in coincidence.
662 A trigger signal was formed using NIM modules from the coincidence of signals from the top

663 and bottom arrays of scintillators. The trigger signal was passed to the front-end electronics
664 attached to the adaptor boards of each layer of the quadruplet.

665 Operating the chambers also required gas and high voltage. A gas mixture of pentane-CO₂
666 in the appropriate proportions was prepared and delivered to each sTGC with a gas system
667 designed and made at McGill University [60]. Since pentane is flammable, the gas system
668 was designed with safety top of mind. The gas system was controlled by a slow control
669 program, also custom made [60]. To prepare the quadruplets for operation, CO₂ was flushed
670 through them overnight to remove potential impurities within each chamber's gas volume.
671 Then, the equivalent of approximately five sTGC gas volumes of the pentane-CO₂ mixture
672 was flushed through to ensure a uniform gas mixture inside the sTGCs; the procedure takes
673 approximately four hours. High voltage was provided by commercial CAEN high voltage
674 boards [60].

675 5.3 Data acquisition

676 Each sTGC electrode was connected to a channel on a prototype ASIC¹ on the front-end elec-
677 tronics, attached to the adaptor boards on each layer of a quadruplet. Each ASIC features
678 64 charge amplifiers with selectable gain and input signal polarities, which output the digi-
679 tized amplitude of the signal at peak for channels above a pre-defined threshold. Thresholds
680 were estimated [62] by optimizing the efficiency of detecting muons while minimizing noise,
681 and further manually tuned in the configuration/readout software before the start of data
682 acquisition for each quadruplet. The signal from the capacitively-coupled strip electrodes
683 has positive polarity and is read out with a gain of one. For each trigger, the signal peak
684 amplitude of all channels above threshold was recorded as an event and stored in a binary
685 file. The readout of strips made use of a special feature of the custom ASIC, the so-called
686 “neighbour triggering” function where signals on channels adjacent to those above threshold
687 are also read out.

688 The quadruplets were held at 3.1 kV for approximately two hours to collect data from
689 approximately 1 million muon triggers.

¹A custom Application Specific Integrated Circuit (ASIC) named VMM3 [61], designed for the readout of signals from the micromegas and sTGCs of the NSWs.

690 **5.4 Data preparation**

691 **5.4.1 Data quality cuts on electrode hits**

692 Corrupted data, if any, is removed while the raw data is being recorded in a binary file. After
693 data taking is completed, the raw data is decoded and the electronics channels are mapped
694 to physical readout electrodes of the quadruplet. The result of this data preparation step is
695 stored in a ROOT [63] tree data format.

696 A hit is defined as a signal recorded from a channel that was above threshold or (in the
697 case of strips) neighbour triggered. In addition to hits from muons, the quadruplets record
698 noise from the electronics and δ -rays (electrons liberated with sufficient energy to escape
699 a significant distance away from the primary radiation and produce further ionization).
700 Therefore, selection cuts are applied to reduce the number of hits that do not originate from
701 muons. Readout strips located at the very edge of the cathode board tend to have higher
702 electronic noise. As a result, all strip hits on a layer where a hit is present on the strips
703 at either edge of the quadruplet are removed from the analysis. A default pedestal value
704 is subtracted from the recorded signal peak amplitude of each electrode for a more realistic
705 estimate of the signal amplitude. Also, events that only have hits on pad electrodes (no
706 strips or wires) were removed from the analysis since these hits are likely from electronic
707 noise, which is higher on the pad readout channels due to their large area.

708 **5.4.2 Clustering and tracking**

709 For events passing the quality selection cuts defined in section 5.4.1, the x - and y -coordinates
710 of the ionization avalanche on each layer are extracted from the signal on the wires and strips
711 respectively for each event, as shown schematically in figure 5.2. In this work, x is defined as
712 the coordinate perpendicular to the wires and y is defined as the coordinate perpendicular
713 to the strips. The z -coordinate is perpendicular to the sTGC surface.

714 The x -coordinate of the muon position is taken as the center of the wire group with the
715 maximum peak signal amplitude, since the wire groups' pitch (36 mm) is larger than the
716 typical extent of the ionization charge generated inside a sTGC. Assuming that the true x -
717 position of the hit is sampled from a uniform distribution over the width of the wire group,
718 the uncertainty in the x -position is approximately $\frac{36}{\sqrt{12}}$ mm = 10 mm [64].

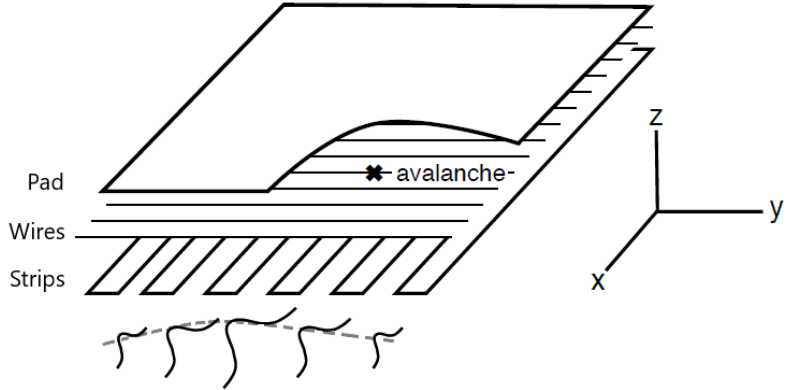


Figure 5.2: Schematic diagram representing the three types of electrodes in a sTGC detector. The position of the ionization avalanche is extracted from the wires and strips that picked up the avalanche signal. The signals on individual strips are sketched. Clustering is the process by which a Gaussian function (represented by the grey dashed line) is fitted to the distribution of the signal amplitude on individual contiguous strips; a sample cluster is shown in figure 5.3. In this work, the $x(y)$ -coordinate will always refer to the coordinate perpendicular to the wires (strips). The z -coordinate is perpendicular to the sTGC surface [58, 56].

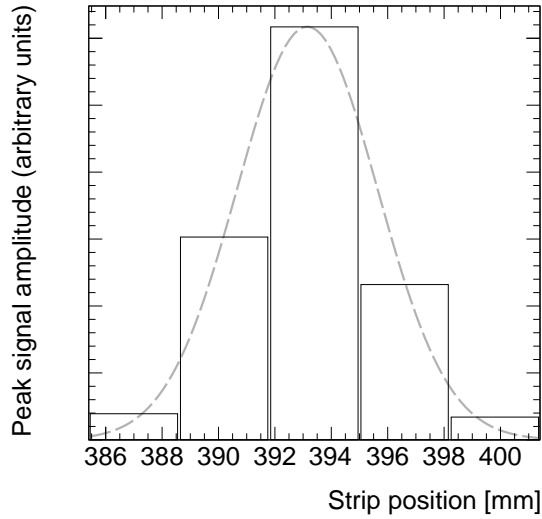


Figure 5.3: A sample cluster resulting from signal recorded on a group of contiguous strips after the passing of a muon. The grey dashed line represents the result of a fit to a Gaussian distribution.

719 The y -coordinate of the muon's position is taken as the Gaussian mean of the peak signal
720 amplitude distribution across a group of contiguous strips that registered hits. The process
721 of grouping contiguous strip hits on a layer is called clustering, and the resulting group is
722 called a cluster. Figure 5.2 sketches the clustering process and a sample cluster is shown
723 in figure 5.3. The data acquisition system recorded the identification number of the strip
724 electrode that was hit and in the clustering process the position of the center of the strip
725 electrode is calculated based on the nominal quadruplet geometry. Typically, clusters are
726 built of 3-5 strips. The thickness of the graphite coating over the cathode boards determined
727 how many strips picked up the ionization image charge. Larger clusters can often originate
728 from δ -rays since they spread the ionization charge over a larger area.

729 Events are removed from further analysis if there are two reconstructed clusters on one sTGC,
730 since some hits could be from electronic noise or a simultaneous second muon traversing the
731 chamber. Clusters are rejected if the cluster size is lesser than three strips (which should
732 not happen for real events thanks to neighbour triggering), and if the cluster size is greater
733 than 25. After all quality selection cuts are applied on hits and clusters, approximately half
734 of the events recorded remain.

735 The uncertainty on the reconstructed cluster position is assessed by comparing the difference
736 between Gaussian means obtained using two different algorithms. As shown in appendix A,
737 the difference between the means from the two algorithms considered is found to be ap-
738 proximately 60 μm on average, larger than the statistical uncertainty on the Gaussian mean
739 obtained from the cluster fit. Therefore, an uncertainty of 60 μm is assigned to the recon-
740 structed y -coordinate of a muon.

741 The reconstructed x and y coordinates on each quadruplet layer are used to reconstruct
742 a straight track, independently, in the x - z and y - z planes. Tracks are reconstructed using
743 muon coordinates for every possible pair of two sTGC layers. For example, if an event has
744 muon coordinates reconstructed on all four layers, a total of six track segments in the x - z
745 plane and six track segments in the y - z plane will be reconstructed.

746 5.5 Relative local offsets

747 The offset of a strip from its nominal position can be modeled as a passive transformation.
748 The *local offset* is defined as the shift in the strip pattern with respect to nominal geometry
749 in a specific area of the sTGC. Local offsets systematically change the set of strips nearest
750 to muons passing through an area. The data preparation software assumes that strips are
751 in their nominal positions, so the recorded y -coordinate of the muon on layer i , y_i , is shifted

752 opposite to the layer's local offset, $d_{local,i}$, by

$$y_i = y_{nom,i} - d_{local,i}, \quad (5.1)$$

753 where $y_{nom,i}$ is the position of the muon that would have been recorded on layer i if there
754 was no local offset. Equation 5.1 ignores other factors that affect the cluster position, like
755 position resolution. With cosmics data, there was no external reference to measure $y_{nom,i}$
756 and the local offset is unknown. Therefore, only relative local offsets can be measured.

757 To measure relative local offsets, two of the four sTGC layers are chosen to provide a reference
758 coordinate system. Relative local offsets are calculated with respect to the two reference
759 or fixed layers. The hits on the two fixed layers were used to create tracks that can be
760 interpolated or extrapolated (polated) to the other two layers. The set of two fixed layers
761 and the layer polated to are referred to as a tracking combination. The residual of track i ,
762 Δ_i , is defined as,

$$\Delta_i = y_i - y_{track,i}, \quad (5.2)$$

763 where $y_{track,i}$ is the polated track position on the sTGC layer the residual is measured on.
764 Track residuals are affected by the local offset in the area of each layer's hit. As an example,
765 in figure 5.4, the residual on layer 2 perhaps indicates that layer 2 is offset with respect to
766 layers 1 and 4 in the area of the track. Of course, a single track residual says nothing of
767 the real relative local offset because of the limited spatial resolution of the detectors and
768 fake tracks caused by noise or delta rays. However, the mean of residuals for all tracks in a
769 region of interest will be shifted systematically by the local offsets between layers [58]. For
770 a quadruplet with nominal geometry, the mean of residuals should be zero in all regions and
771 for all reference frames, unlike the example regions in figure 5.5. The value of the mean of
772 residuals is a measure of the relative local offset of the layer with respect to the two fixed
773 layers used to reconstruct the muon track. The sign convention is such that the mean of
774 residuals is opposite to the relative local offset.

775 To study the relative local offsets, residual distributions across each strip layer of a quadruplet
776 for all possible tracking combinations are assembled and fitted. As expected, the residual dis-
777 tributions are wider for tracking combinations where the extrapolation lever arm is largest,
778 as in the example distributions shown in figure 5.5. In general, residual means from dis-
779 tributions of residuals with geometrically less favourable tracking combinations have larger
780 statistical and systematic uncertainties. The bin size of 200 μm for the distributions shown
781 in figure 5.5 was chosen based on the uncertainty on residuals calculated from tracks on layer
782 4 (1) built from hits on layers 1 and 2 (3 and 4) given a cluster y -coordinate uncertainty
783 of 60 μm (discussed in section 5.4.2 and appendix A), since these tracks yield residuals with
784 the largest uncertainties.

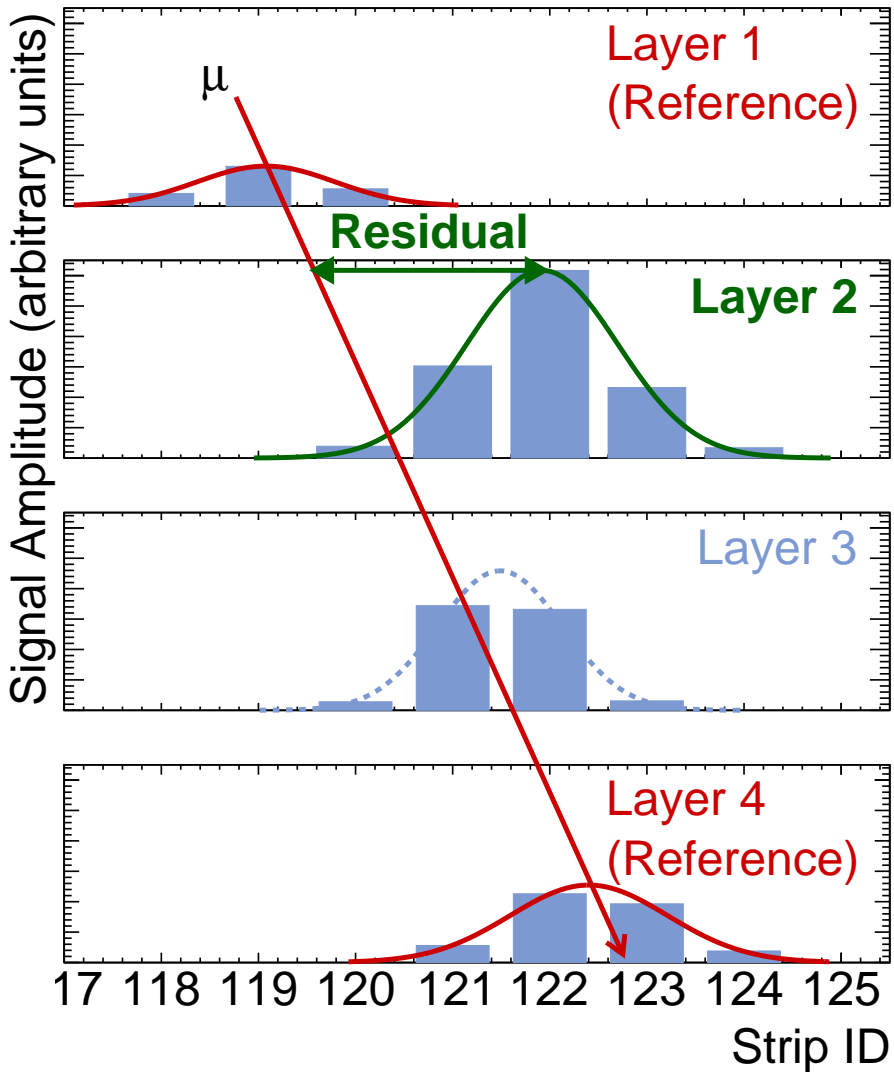
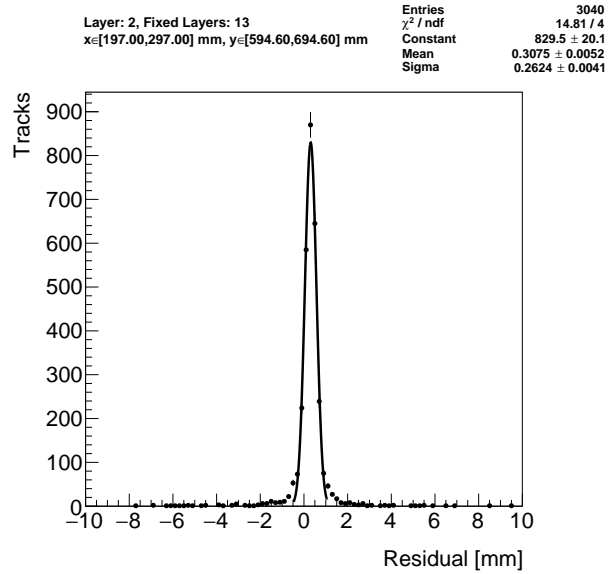
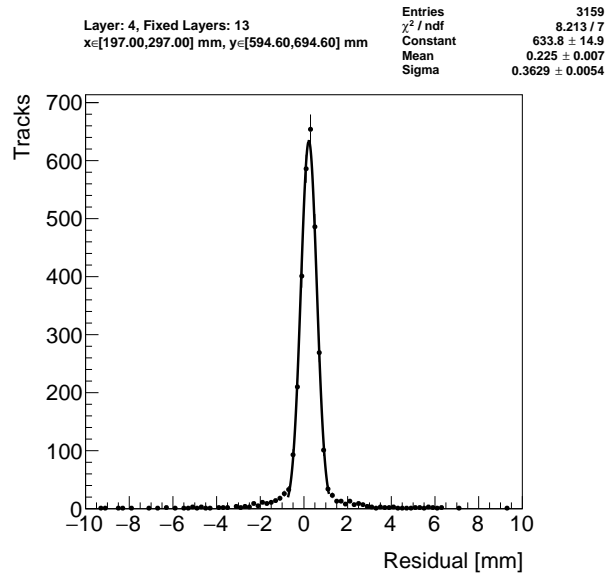


Figure 5.4: Representation of a muon event recorded by an sTGC quadruplet. The charge clusters measured using strip electrodes are fit with a Gaussian distribution and the fitted mean is taken as the reconstructed muon position. A track is built from the chosen reference layers, 1 and 4, and the track residual is calculated on layer 2. The clusters come from a real muon, but their positions were modified to highlight the non-zero value of the residual on layer 2.



(a) Tracks on layer 2, reference layers 1 and 3.



(b) Tracks on layer 4, reference layers 1 and 3.

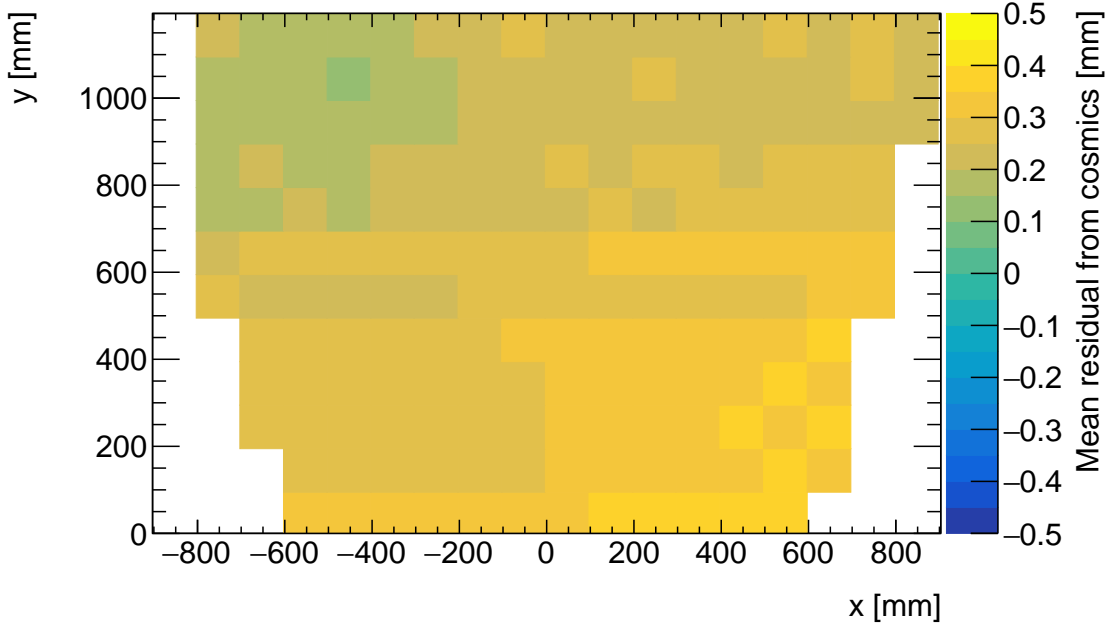
Figure 5.5: Residual distribution in the region $x \in [197, 297]$ mm, $y \in [594.6, 694.6]$ mm (100 mm by 100 mm area) for two different tracking combinations. Data from quadruplet QL2.P.11.

785 A Gaussian fit is used to extract the mean of the residual distributions. The residual distri-
786 butions are actually better modeled by a double Gaussian distribution, which better captures
787 the distribution tails in figure 5.5. However, a study described in appendix C.1 found that
788 a fit to a single Gaussian function in the core of the distribution is sufficient to reconstruct
789 the mean of the distribution.

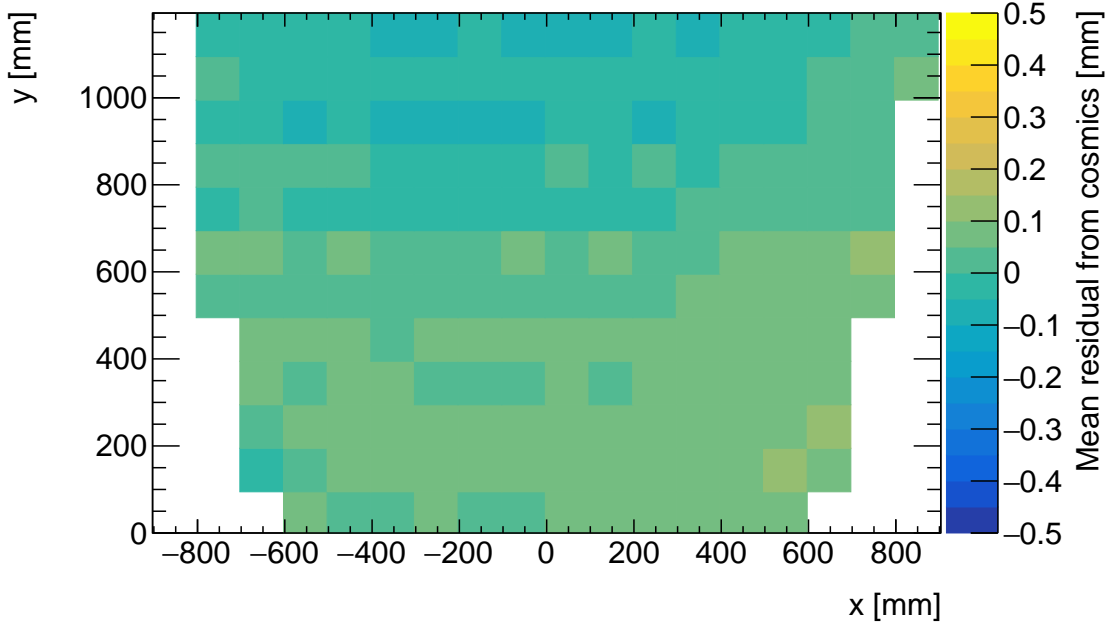
790 The area of the region of interest where tracks residuals were included in the residual distri-
791 bution was 100 mm by 100 mm. The size balanced the number of tracks falling in the region
792 of interest to give a small statistical uncertainty on the fitted mean while being smaller
793 than the order on which local offsets were expected to change significantly. “Significantly”
794 was defined as 100 μm , the required position resolution of the sTGCs and the precision to
795 which strip positions should be known. The distance over which local offsets are expected to
796 change significantly can be estimated using a simple alignment model. Assuming the strips
797 of a layer have been displaced uniformly from their nominal positions by a global offset and
798 rotation, the distance in x that a large but possible rotation of 1 mrad changes the local
799 offset by 100 μm is 100 mm.

800 The means of residuals are plotted across each sTGC layer for every possible tracking combi-
801 nation to get a picture of the how the relative local offsets change as a function of position
802 over the layer’s surface. Figure 5.6 shows the mean of residuals on layer 2 calculated with
803 layers 1 and 3 as reference for two different quadruplets, referred to as QL2.P.11 and QL2.P.8.
804 In figure 5.6a, the Gaussian mean of the residual distribution in figure 5.5a is the entry in
805 the bin defined by the boundaries $x \in [197, 297]$ mm, $y \in [594.6, 694.6]$ mm.

806 Many of the residual means are non-zero and change smoothly over layer 2, indicating that
807 there are relative local offsets stemming from global misalignments between the strip patterns
808 of different sTGC layers in both quadruplets. Given that the residual mean changes with x in
809 figure 5.6a, quadruplet QL2.P.11 likely has a rotation of layer 2 with respect to layers 1 and
810 3, combined with an offset of the entire layer. The residual means are smaller in figure 5.6b
811 indicating that quadruplet QL2.P.8 is less misaligned overall than QL2.P.11; however, the
812 relative local offsets range between $\pm 200 \mu\text{m}$ so they are significant enough to warrant a
813 correction so the quadruplet can achieve the required track angular resolution in the NSW.



(a) Mean of track residuals on layer 2, obtained using layers 1 and 3 as reference, for QL2.P.11.



(b) Mean of track residuals on layer 2, obtained using layers 1 and 3 as reference, for QL2.P.8.

Figure 5.6: Mean of residuals in each 100 mm by 100 mm bin over the area of sTGC layer 2 for quadruplets QL2.P.11 and QL2.P.8. The entry in $x \in [197, 297]$ mm, $y \in [594.6, 694.6]$ mm of figure 5.6a corresponds to the fitted Gaussian mean in figures 5.5a. The mean of residuals has the same value and opposite sign to the relative local offset of layer 2 with respect to the reference frame defined by layers 1 and 3.

814 5.6 Systematic uncertainty

815 The statistical uncertainty on the local residual means was typically around 10 - 20 μm , and
816 appendix B shows that the analysis is not statistically limited by the number of triggers
817 collected for each quadruplet. Systematic uncertainties were found to be larger than the
818 statistical uncertainty on the residual means.

819 Several analysis choices had some degree of impact on the fitted means of local track residual
820 distributions. To study the impacts, the residual means were calculated in different ways and
821 distributions of the differences made. The complete studies are shown in appendix C. The
822 root-mean-square (RMS) of the residual mean difference distributions were used to quantify
823 the impact of the different analysis choices as systematic uncertainties on the residual means.
824 The following analysis choices are considered:

- 825 • The impact of performing a single or double Gaussian fit on the track residual distri-
826 butions is studied. As shown in appendix C.1, the difference between fitting the track
827 residual distribution with a single or double Gaussian function varies between 10-30 μm
828 from the most to least geometrically favourable tracking combinations.
- 829 • The impact of the operating voltage used during data taking is investigated. Cosmic
830 muon data was recorded at 2.9 kV and 3.1 kV. As described in appendix C.2, an
831 uncertainty between 10-40 μm is assigned to the different tracking combinations.
- 832 • The impact of using different Gaussian fitting algorithms used to reconstruct the po-
833 sition of a charge cluster was considered. Clusters are fit with the Minuit2 [65] and
834 Guo's method [66]. As shown in appendix C.3, the resulting difference in residual
835 means is between 10-30 μm from the most to least geometrically favourable tracking
836 combinations.
- 837 • The impact of correcting reconstructed cluster positions for differential non-linearity
838 (DNL) is studied. DNL is fully described in appendix C.4. It is a bias in the recon-
839 structed cluster position that comes from discretely sampling a continuous distribu-
840 tion, in this case the charge distribution [67, 58, 6]. The difference between residual
841 means is compared with and without correcting the reconstructed cluster positions.
842 Appendix C.4 shows that the impact of the correction is smaller than 10 μm for all
843 tracking combinations, which is almost negligible.

844 A summary of the systematic uncertainties assigned to the local means of residuals for each
845 tracking combination is given in table 5.1. The RMS of the distributions of residual mean
846 differences of geometrically similar tracking combinations are averaged and the average value

Tracking geometry	Residual distribution fit function (C.1)	Cosmics data collection voltage (C.2)	Cluster fit algorithm (C.3)	Apply DNL correction or not (C.4)	Total
Similar to layer 3, fixed layers 1, 2	0.01 mm	0.04 mm	0.02 mm	0.01 mm	0.05 mm
Similar to layer 4, fixed layers 1, 2	0.03 mm	0.01 mm	0.03 mm	0.01 mm	0.10 mm
Similar to layer 2, fixed layers 1, 3	0.01 mm	0.02 mm	0.01 mm	0.000 mm	0.03 mm
Similar to layer 4, fixed layers 1, 3	0.01 mm	0.04 mm	0.01 mm	0.01 mm	0.04 mm
Similar to layer 2, fixed layers 1, 4	0.01 mm	0.04 mm	0.01 mm	0.01 mm	0.04 mm

Table 5.1: Systematic uncertainty assigned for each analysis option, detailed in appendix C.

847 is taken as the systematic uncertainty for those tracking combinations. An example of a ge-
 848 ometically similar pair of tracking combinations is fixing layers 1 and 2 and extrapolating
 849 to layer 3 or fixing layers 2 and 3 and extrapolating to layer 4; geometrically similar combi-
 850 nations have the same polation lever arm. The total systematic uncertainty is obtained by
 851 summing in quadrature all the different sources of systematic uncertainty. The uncertainty
 852 in each mean of residuals is obtained by summing in quadrature the statistical uncertainty
 853 in the mean of residuals and the appropriate systematic uncertainty for the tracking com-
 854 bination used to calculate the mean of residuals.

855 5.7 Discussion

856 The total uncertainty in the residual means, and hence the relative local offsets, is typically
 857 less than the design sTGC position resolution of $\sim 100 \mu\text{m}$ [5]. Therefore, the residual means
 858 are relevant input for alignment studies.

859 The relative local offsets calculated from the means of residual distributions over the surface
860 of an sTGC layer for all tracking combinations provide a complete picture of the relative
861 alignment between sTGC layers in a quadruplet module. In fact, cosmic muon testing is the
862 only characterization technique where the entire surface of quadruplet layers can be probed
863 since muons hits are distributed almost uniformly; the CMM [7] and x-ray methods [8]
864 depend on measurements at reference points, and test beams only have a limited beam spot
865 to work with [6]. By looking at 2D-histograms of residual means like figure 5.6 for all tracking
866 combinations, it is easy to identify quadruplets that suffer large relative misalignment since
867 many residual means differ significantly from zero. Moreover, the pattern in the residual
868 means can be used to motivate a physical interpretation of misalignments. The residual
869 means can be used as a reference, cross check, or input to other alignment studies.
870 Relative local offsets cannot be used to position strips in the absolute ATLAS coordinate
871 system because there is no external reference to measure positions on all layers with respect
872 to. The lack of an external absolute reference frame means that there is not enough infor-
873 mation to unfold relative local offsets into absolute local offsets (with respect to the nominal
874 quadruplet geometry). As an example, assuming that the residual on layer 2 in figure 5.4 is
875 representative of the absolute value of the relative local offset, the residual on layer 2 could
876 be caused by the strips on layer 2 being misaligned from nominal, but it could also be caused
877 by strips on layers 1 and 4 being offset from nominal while the strips on layer 2 are in their
878 nominal positions! Any number of combinations of local offsets on layers 1, 2 and 4 could
879 produce the residual on layer 2. Absolute local offsets must be calculated using another
880 method: the x-ray method.

881 **Chapter 6**

882 **Using x-rays to measure relative strip
883 position offsets**

884 Local offset measurements were done with the x-ray method. The reader is referred to the
885 paper describing the x-ray method [8], although some minor changes have been made to the
886 experimental setup since it was written. The experimental setup described here is current
887 and was used to collect the data presented in this thesis.

888 **6.1 Experimental setup**

889 The x-ray tests were performed after the quadruplets arrived at CERN, were assembled into
890 wedges, and alignment platforms installed. Essentially, an x-ray gun was attached to one
891 of the alignment platforms glued to the surface of the wedge and the x-ray beam profile
892 recorded by the strips.

893 The wedges were installed on carts that could rotate their surface to a horizontal position. A
894 mounting platform was installed on top of the alignment platform using a three-ball mount.
895 The x-ray gun used was an [Amptek Mini-X tube](#). The gun was placed in a brass holder
896 with built-in 2 mm collimator and 280 μm copper filter. The holder was mounted on one
897 of five positions on the mounting platform, as shown in figure 6.1. Gun positions were
898 chosen to avoid wire support structures in the sTGCs that reduce hit efficiency [58] and
899 boundaries between sets of strips read out by two different ASICs that could each have
900 different thresholds.

901 As with cosmics data collection, each sTGC also needed gas and high voltage to operate.

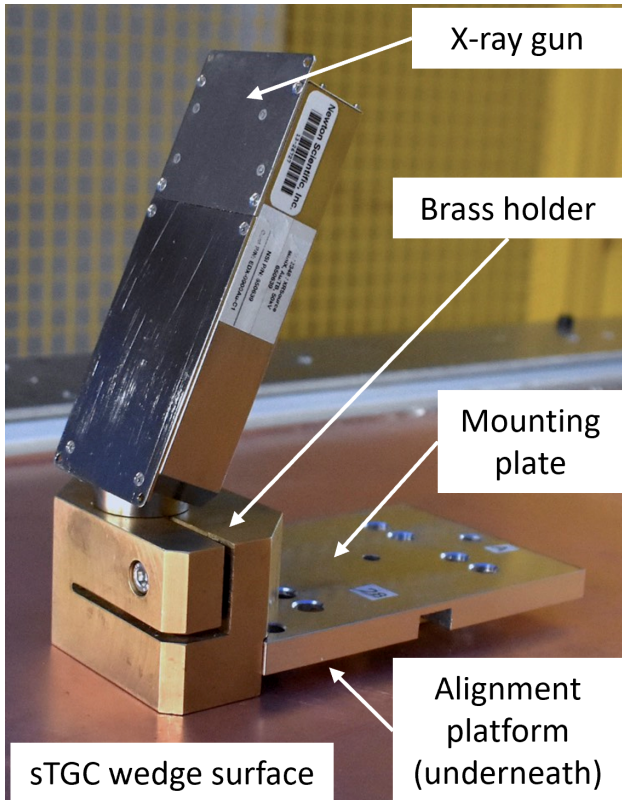


Figure 6.1: The x-ray gun mounted to the alignment platform on the surface of the wedge. Adapted from [8].

- 902 Each layer was operated at 2.925 kV with high voltage from a NIM crate. The chambers
903 were flushed with CO₂ before and during data collection.
- 904 The gun produced x-rays with energies under 40 keV with peaks in the 7-15 keV range. Peaks
905 in the 0-30 keV range were filtered out by the copper filter and the copper of the sTGCs.
906 The x-rays mostly interacted with the wedge's copper electrodes and gold-plated tungsten
907 wires via the photo effect. The resulting photoelectrons caused ionization avalanches that
908 were picked up by the strips.

909 6.2 Data acquisition

- 910 A different version of the same front end electronics, but the same ASIC, as used in cosmics
911 testing were used for the x-ray testing to amplify the electrode signals and measure the peak

912 signal amplitude. Data was collected for two minutes per gun position with random triggers.
913 A trigger recorded all signals above threshold. Pad and wire data was not recorded.

914 6.3 Data preparation

915 Like with cosmics analysis, a default pedestal is subtracted from the signal peak amplitude
916 on each electrode.

917 Clusters are defined as groups of contiguous strip hits collected within 75 ns. The peak signal
918 amplitude of each electrode in a cluster is fit with a Gaussian, and the mean of the Gaussian
919 is taken as the cluster position. Cluster positions are corrected for DNL (see definition in
920 appendix C.4). Only clusters composed of hits on 3-5 strips were used in the x-ray analysis.
921 Clusters with signal on more than 5 strips were cut because they were most likely caused by
922 photoelectrons ejected with enough energy to cause more primary ionization and subsequent
923 avalanches as δ -rays.

924 The x-ray analysis diverges entirely from the cosmics analysis algorithm here because the x-
925 rays do not leave tracks. The signals picked up by the strips are from ionization avalanches [54]
926 generated by photoelectrons liberated from the metals of the sTGCs, which only travel
927 through one gas volume and are ejected at all angles. Instead of creating tracks, the cluster
928 position distribution on each layer is used to define the beam profile. A typical beam profile
929 is shown in figure 6.2.

930 6.4 Measuring local offsets

931 The mean of the cluster position distribution is taken as the x-ray beam profile center. The
932 expected center is calculated for each gun position using the nominal quadruplet geometry
933 parameters. The nominal position is corrected for the geometry of the brass holder and the
934 positioning and angle of the alignment platforms and the beam angle. The difference between
935 the expected and reconstructed beam profile center is a measure of the local offset. Applying
936 the logic of equation 5.1 to the beam profile, the Gaussian mean of cluster positions on the
937 given layer acts as the recorded position, y_i , the expected center is $y_{nom,i}$ and the local offset
938 is $d_{local,i}$ as before, where i denotes the layer. Since the position of the alignment platforms
939 will be monitored by the alignment system in ATLAS [5], the position of the strips that
940 should have been at the gun position are shifted by $d_{local,i}$ and so are known in the ATLAS
941 coordinate system for every position where x-ray data was taken.

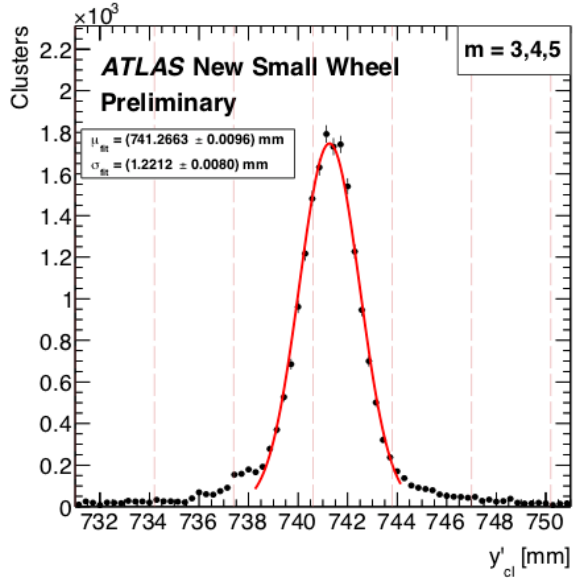


Figure 6.2: Distribution of x-ray cluster mean positions after the analysis cuts and corrections. The strip cluster multiplicity, m , was limited to 3, 4 and 5. The red curve is a Gaussian fit of the distribution and the pink dashed lines denote the edges of the strips [8].

- 942 The x-ray working group accepted an uncertainty of $120 \mu\text{m}$ on the beam profile centers. The
 943 largest uncertainty comes from the effect of the gun angle, which proved difficult to measure
 944 and correct for.
 945 The local offsets are not presented here as the author did not conduct this work. However,
 946 the author used the local offsets to calculate relative local offsets.

947 6.5 Measuring relative local offsets

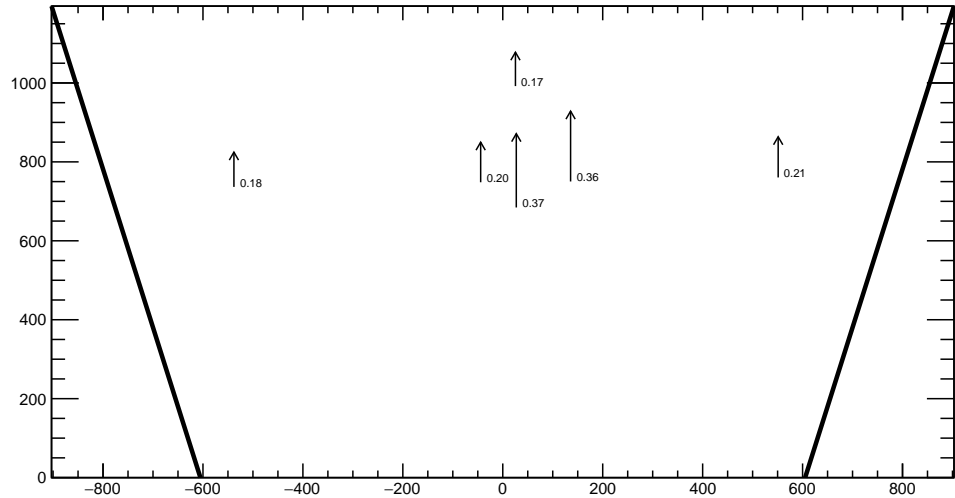
- 948 The x-ray local offsets were shown to be correlated with the local offsets calculated from
 949 the CMM data, but the CMM data does not include the effect of inter-layer misalignments
 950 so the degree of correlation measurable was limited. Cosmics data is affected by inter-layer
 951 misalignments. Since the local offsets for x-rays and cosmics data are measured in different
 952 coordinate systems, they cannot be compared directly. Bringing the cosmics relative local
 953 offsets into an absolute coordinate system is impossible; however, the x-ray local offsets can
 954 be brought into a relative coordinate system.
 955 The measured x-ray beam profile centers were systematically affected by local offsets in the

same way as the mean cosmics residuals, as modeled by equation 5.1. Therefore, if a 2-layer track is built from the beam profile centers on each layer and the residual calculated on a third layer, that residual should match the local mean cosmics residual. The residual is the difference between the beam profile center on the layer of interest and the polated track position from the beam profile centers recorded on the two fixed layers. The beam profile center on the layer of interest acts as y_i and the polated track position acts as $y_{track,i}$ in equation 5.2.

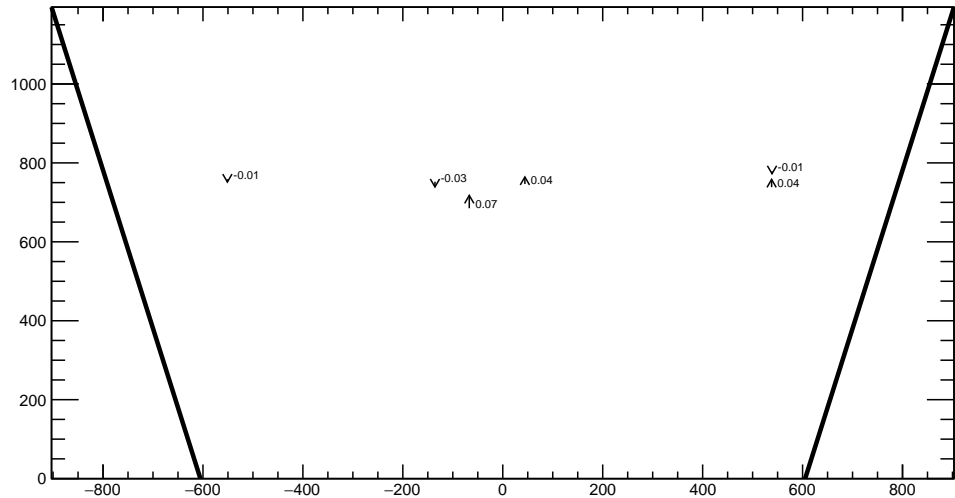
The track referred to here is not an actual track of the x-ray beam. A beam profile center is actually the Gaussian mean of all selected mean cluster positions recorded during the x-ray data taking period, not a single hit of a track. Building an “abstract” track was necessary because the x-rays cause signal in the chamber via the photoeffect so there were not individual “x-ray tracks” to record. In fact the x-ray data could be collected separately for each layer. Nonetheless, since the effect of local offsets on the beam profile centers was the same as their effect on the cosmics cluster positions the difference in algorithm between x-ray and cosmics analysis was allowed.

For each x-ray survey position, the x-ray residual was calculated for all possible tracking combinations (which required an x-ray beam profile on at least three layers). The x-ray residuals on layer 2 calculated from the beam profile centers recorded on layers 1 and 3 are represented as arrows for QL2.P.11 and QL2.P.8 in figure 6.3. For QL2.P.11, a negative relative local offset at all x-ray survey positions is clear.

The uncertainty on the x-ray residuals was the error propagated through the tracking, taking an uncertainty of 120 μm on each beam profile center. The uncertainty on the x-ray residuals ranged from 0.15 mm to 0.4 mm from the most to least geometrically-favourable tracking combination. There is no discernible pattern to the x-ray residuals on QL2.P.8 because they have absolute values smaller than the uncertainty on the x-ray residuals. The x-ray residual uncertainties are significantly larger than the uncertainties on the mean cosmics residuals.



(a) QL2.P.11 x-ray residuals on layer 2, reference layers 1 and 3.



(b) QL2.P.8 x-ray residuals on layer 2, reference layers 1 and 3.

Figure 6.3: The x-ray residuals on layer 2 calculated from the beam profile centers recorded on layers 1 and 3 for QL2.P.11 and QL2.P.8. The arrows originate from the expected position of the beam profile center assuming a nominal geometry, and the lengths are proportional to the calculated x-ray residuals. The value of the x-ray residuals are annotated in millimeters and have an uncertainty of ± 0.15 mm.

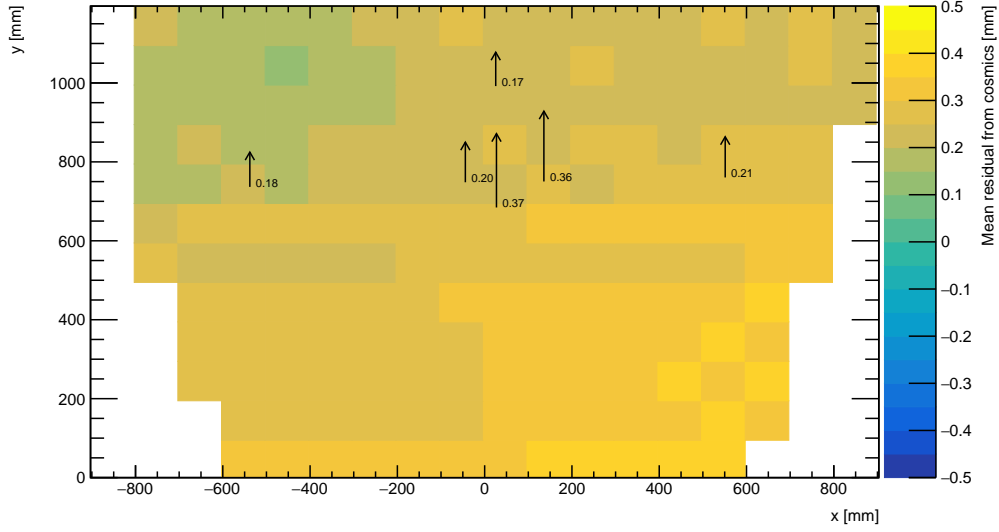
982 **Chapter 7**

983 **Comparing cosmic muon and x-ray
984 relative strip position offsets**

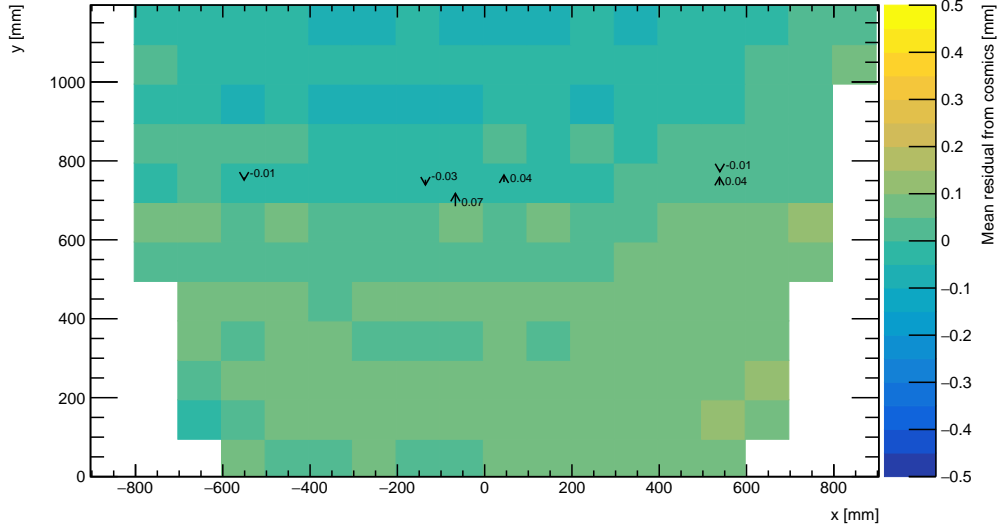
985 The goal was to validate the local offsets extracted from the x-ray data with cosmics data.
986 The complication was that the x-ray dataset provided absolute local offsets while the cosmics
987 dataset provided relative local offsets, which could not be compared directly. The solution
988 was to use the x-ray local offsets to calculate relative local offsets. The x-ray relative local
989 offset is opposite sign to the x-ray residual reconstructed from an abstract track using the
990 beam profile centers on each layer as the track hits. The cosmics relative local offset was
991 inferred from the Gaussian mean of muon track residuals in a 100 mm by 100 mm area,
992 referred to the as the mean cosmics residual. Residuals of each type calculated using the
993 same reference layers are compared for each area where x-ray data is available. The results
994 of the comparison are presented here.

995 **7.1 Assessing correlation**

996 The 2D visualizations of the mean cosmics and x-ray residuals for tracks on layer 2 with
997 reference layers 1 and 3 on QL2.P.11 and QL2.P.8 are shown in figure 7.1. Figure 7.1 is a
998 superposition of figures 5.6 and 6.3.



(a) QL2.P.11 residuals of tracks on layer 2, reference layers 1 and 3.



(b) QL2.P.8 residuals of tracks on layer 2, reference layers 1 and 3.

Figure 7.1: The mean cosmics residuals are shown using colour. The x-ray residuals available at nominal gun positions are drawn as arrows and the value of the residual annotated in millimeters with uncertainty ± 0.15 mm. The length of the arrows is 500 times the value of the x-ray residual, scaled for visibility. These plots are a superposition of figures 5.6 and 6.3.

999 Figure 7.1a shows that for QL2.P.11 the x-ray residuals are of the same sign and order as the
1000 mean cosmics residuals, as can be seen by comparing the the annotated value of the x-ray
1001 residual to the mean cosmics residual represented by colour; QL2.P.11's mean cosmics and x-
1002 ray residuals are correlated to some degree. For QL2.P.8, the x-ray residuals are of the right
1003 order compared to the mean cosmics residuals, but the correlation is not apparent. While
1004 x-ray residuals do not reveal a pattern in relative local offset across the layer's surface, the
1005 mean cosmics residuals show a structure to the relative local offsets since they vary smoothly
1006 over the surface of layer 2.

1007 The comparison of mean cosmics and x-ray residuals was done for several quadruplets for all
1008 tracking combinations (not just layer 2 residuals calculated with fixed layers 1 and 3 like in
1009 figure 7.1). Scatter plots of the x-ray and mean cosmics residuals on QL2.P.11 and QL2.P.8
1010 for all tracking combinations shown in figures 7.2 and 7.3 reveal the degree of correlation
1011 between the datasets. In the correlation plots, each rectangle is centered on the value of a
1012 mean cosmics and x-ray residual pair calculated with a given tracking combination for every
1013 gun position where data is available; the height and width of the squares are the uncertainty
1014 in the mean cosmics and x-ray residuals respectively. Note that in the scatter plots, the
1015 regions of interest where cosmics tracks are included in the calculation of mean of residuals
1016 are exactly centered on the nominal x-ray beam position, unlike in figure 7.1.

1017 The fitted slope and offset in figure 7.2 show that the two QL2.P.11 datasets are correlated.
1018 The large uncertainty on the x-ray residuals set a limit on the sensitivity of the analysis,
1019 for if the absolute value of the x-ray residuals of a quadruplet were smaller than the x-ray
1020 residual uncertainties, no conclusion about the correlation could be drawn, like for QL2.P.8
1021 (figure 7.3). This result is reflected in the small x-ray residuals shown in figure 7.1b that
1022 do not reveal a pattern in the relative local offsets across the surface of layer 2. However,
1023 figure 7.3 shows that the x-ray and mean cosmics residuals are clustered around zero, as is
1024 expected for a quadruplet with small relative misalignments between layers.

1025 There are three patterns in the residuals on the scatter plot explained by geometry. First,
1026 for both datasets the uncertainty in the extrapolated track residuals were larger than the
1027 interpolated track residuals because of the extrapolation lever arm. For the x-ray residuals,
1028 the effect of the lever arm on the uncertainty was direct since the residual was calculated from
1029 a single abstract track; for the mean cosmics residuals it was the widening of the residual
1030 distribution due to the extrapolation lever arm that increased the uncertainty in the fitted
1031 mean of residuals. Second, residuals calculated through extrapolation tend to be larger
1032 because the extrapolation lever arm can produce more extreme values of the track position
1033 on the layer of interest. Third, the points in figure 7.2 are geometrically correlated (e.g.
1034 they seem to be roughly mirrored around the origin). This is expected since the residuals
1035 calculated using a given set of three layers should be geometrically correlated by the local

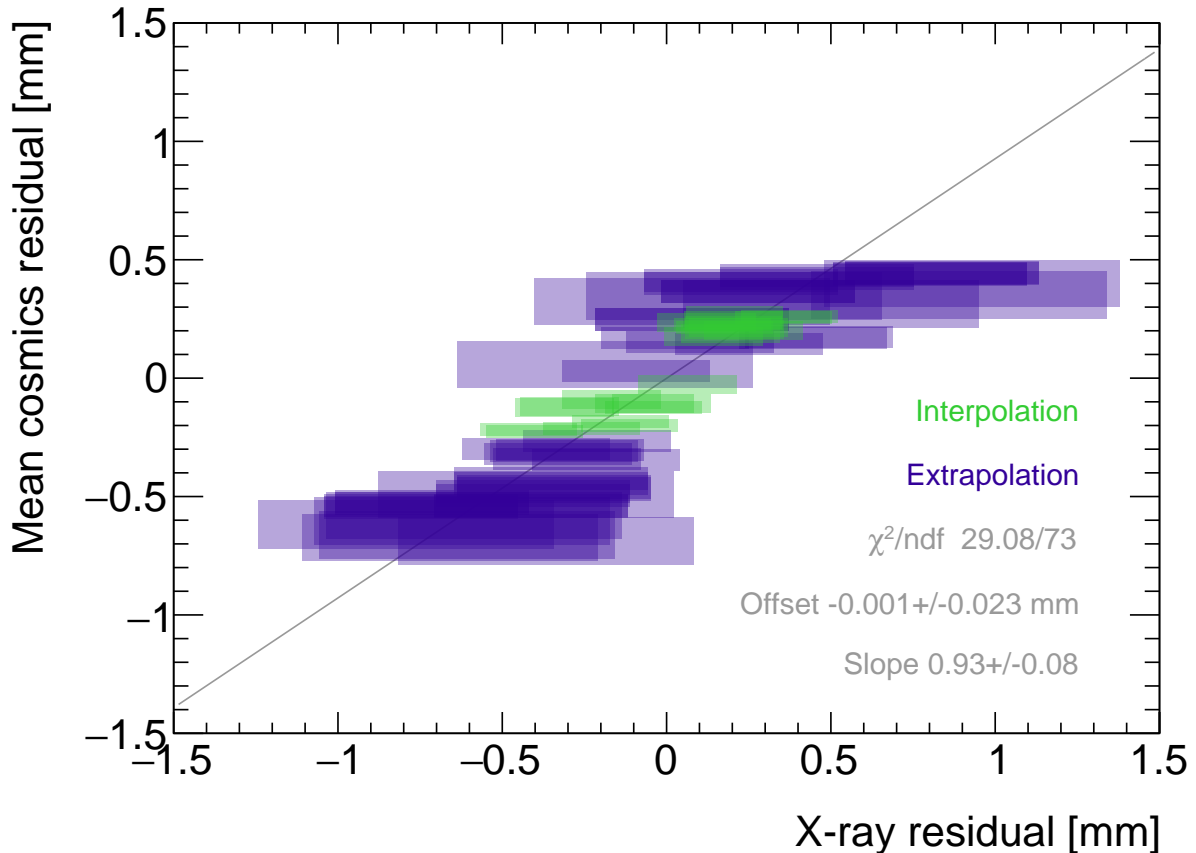


Figure 7.2: Correlation plot between x-ray and mean cosmics residuals for all tracking combinations for QL2.P.11. Each rectangle is centered on an x-ray and mean cosmics residual pair calculated at a given gun position and for a certain tracking combination. The width of the rectangles in x and y are the uncertainty in the x-ray and mean cosmics residual respectively. A printer-friendly version of this plot is available in appendix D.

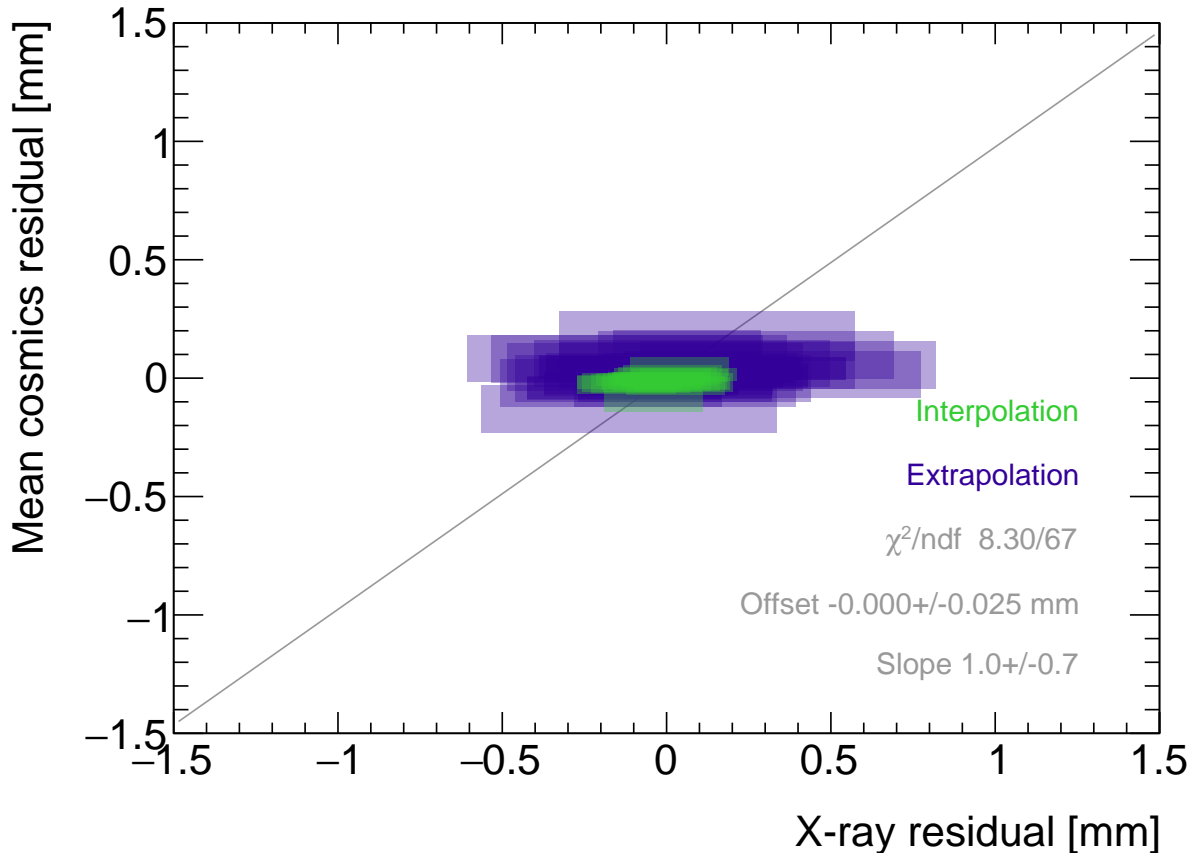


Figure 7.3: Correlation plot between x-ray and mean cosmics residuals for all tracking combinations for quadruplet 2. Each rectangle is centered on an x-ray and mean cosmics residual pair calculated at a given gun position and for a certain tracking combination. The width of the rectangles in x and y are the uncertainty in the x-ray and mean cosmics residual respectively. A printer-friendly version of this plot is available in appendix D.

₁₀₃₆ offsets on each layer (the $d_{local,i}$ on each layer as defined in equation 5.1).

₁₀₃₇ 7.2 Discussion

₁₀₃₈ Several quadruplets were tested for each quadruplet construction geometry built in Canada.
₁₀₃₉ Each quadruplet fell into one of the two categories: residuals large enough to see a correlation,
₁₀₄₀ or residuals too small to see a correlation. Since the x-ray and mean cosmics residuals can
₁₀₄₁ be used to calculate relative local offsets between the layer and the two reference layers,
₁₀₄₂ quadruplets with the largest relative misalignments had the largest range of residuals. The
₁₀₄₃ correlation plots are another easy visual way to identify quadruplets with large relative
₁₀₄₄ misalignments.

₁₀₄₅ The most significant limit on measuring the degree of correlation between the x-ray and
₁₀₄₆ mean cosmics residuals was the uncertainty on the x-ray residuals, which stemmed from the
₁₀₄₇ systematic uncertainty of 120 μm in the x-ray beam profile centers used to build the abstract
₁₀₄₈ tracks. For example, in figure 7.3, if the x-ray residuals could be known to within better
₁₀₄₉ precision, perhaps they would be correlated with the mean cosmics residuals. The x-ray
₁₀₅₀ method was limited primarily by the systematic uncertainties in the relative alignment of
₁₀₅₁ the platforms and the gun, especially the gun angle.

₁₀₅₂ The analysis of certain quadruplets was limited by the availability of data. Sometimes,
₁₀₅₃ less than three layers were surveyed for a given x-ray gun position so no residuals could
₁₀₅₄ be calculated. Too few x-ray residuals prevented the analysis from detecting a significant
₁₀₅₅ correlation, should it even be measurable. Often, the analysis of smaller quadruplets (placed
₁₀₅₆ innermost on the wheel) suffered as a result because they had fewer alignment platforms, and
₁₀₅₇ hence gun positions, on their surfaces. The analysis was also limited to certain quadruplets.
₁₀₅₈ The wedges constructed the earliest (typically small wedges) were surveyed when the x-ray
₁₀₅₉ method was still being designed and so have limited x-ray residuals calculated from beam
₁₀₆₀ profiles of lower quality. In addition, not all cosmic muon test sites had enough front end
₁₀₆₁ electronics to collect data on three layers simultaneously, which is the minimum required to
₁₀₆₂ be able to calculate residuals.

₁₀₆₃ Nonetheless, the comparison of x-ray and cosmics residuals was really to confirm the x-ray
₁₀₆₄ method's ability to measure local offsets with an independent dataset. The x-ray local offsets
₁₀₆₅ allow the calculation of relative local offsets that have been correlated to the cosmics relative
₁₀₆₆ local offsets. Therefore, the analysis of quadruplets with relative local offsets large enough
₁₀₆₇ to detect a correlation validates the x-ray method's ability to measure local offsets.

₁₀₆₈ The potential of using relative local offsets calculated from cosmics data to study relative
₁₀₆₉ alignment between sTGC layers stands on its own. For example, although the x-ray residuals

1070 in QL2.P.8 in figure 7.1b do not reveal a pattern, the variation in the mean cosmics residuals
1071 do. Identifying the pattern is possible because mean cosmics residuals can be calculated
1072 across the entire area and are sensitive to smaller relative local offsets since their uncertainty
1073 is significantly smaller.

1074 The advantage of the x-ray dataset over the cosmics dataset is that absolute local offsets
1075 are measurable thanks to the reference frame provided by the alignment platforms. This is
1076 required to measure the position of strips in the ATLAS coordinate system and to satisfy the
1077 NSWs' precision tracking goals. The x-ray local offsets are being used to build an alignment
1078 model of strips in each quadruplet. It is compelling to imagine using the cosmics relative
1079 local offsets to improve the model considering their precision and ability to capture effects
1080 across the entire area of the quadruplet.

1081 **Chapter 8**

1082 **Outlook and summary**

1083 The cosmic muon dataset was used to independently confirm the local offsets measured by
1084 the x-ray method. The x-ray offsets are being used to complete the sTGC alignment scheme
1085 of the NSWs: the NSW alignment system monitors the position of alignment platforms
1086 on the surface of sTGC wedges, and the x-ray measurements provide the offsets of the strip
1087 pattern with respect to each alignment platform. The continuation of this analysis is detailed
1088 next (section 8.1) before summarizing and considering the larger context (section 8.2).

1089 **8.1 Outlook**

1090 Next all quadruplets with suitable cosmics and x-ray data should be surveyed to flag anomalous
1091 quadruplets (as a first step). If a quadruplet's correlation plot like figure 7.2 or 7.3
1092 reveals an unexpected correlation or has a large scatter, it would indicate an issue with either
1093 the cosmics or x-ray data collection to be investigated further. The uncertainty in each
1094 set of tracking points would inform the interpretation of the anomaly. Then, the quality of
1095 the correlation should be evaluated over all quadruplets instead of individually.

1096 For now, the correlation of the individual quadruplets tested support the use of the x-ray
1097 data to build an alignment model [8]. Work on creating an alignment model is ongoing.
1098 Currently, the algorithm compares the offsets of a local group of strips at each x-ray gun
1099 position as measured by the x-ray and CMM methods in a fit to extract a global slope (m)
1100 and offset (b) per layer, i , where the χ^2 is given by equation 8.1.

$$\chi^2 = \frac{[dy_{cmm,corr} - dy_{xray}]^2}{\delta dy_{xray}^2 + \delta dy_{cmm,corr}^2}, \quad (8.1)$$

1101

$$dy_{cmm,corr} = y_{cmm} + b_i + m_i x - y_{nom} \quad (8.2)$$

1102 Here, dy is an offset as calculated from the x-ray and corrected CMM data and δdy refers
 1103 to their respective uncertainties. The CMM measurements were taken before the cathode
 1104 boards were assembled into quadruplets, so alignment parameters for the given layer were
 1105 extracted from the χ^2 fit by stepping the corrected CMM y -position towards the x-ray y -
 1106 position by adjusting the layer's slope and offset parameters. The plan is that the alignment
 1107 parameters will be provided to the ATLAS experiment's offline software to reconstruct muon
 1108 tracks from the NSWs' sTGCs. The large uncertainty on the x-ray local offsets (120 μm) and
 1109 the sparseness of the measurements means that including input from other characterization
 1110 datasets could reduce the uncertainty on the alignment model parameters.

1111 The uncertainty in the mean cosmics residuals was smaller than the desired position reso-
 1112 lution of the sTGCs, so they provide relevant information about strip positions. Moreover,
 1113 they can be calculated over the entire area of the quadruplet instead of at specific posi-
 1114 tions. It would be great to use the cosmics residuals as input to calculate and reduce the
 1115 uncertainty on the alignment parameters. Since mean cosmics residuals can only provide
 1116 relative alignment information, one idea would be to use them to constrain the fit of the
 1117 alignment parameters. In this case, the alignment parameters would need to be fitted on all
 1118 layers at once, and the shifting y -positions on each layer forced to create an abstracted track
 1119 residual equal to the local mean cosmics residual (within uncertainty) for each x-ray point.
 1120 Or, instead of constraining the fit, it could be penalized if the resulting parameters do not
 1121 result in abstracted track residuals equal to the mean cosmics residuals within uncertainty.
 1122 Some work on using the three datasets at once in a fit has been started.

1123 8.2 Summary

1124 The LHC [1] will be at the energy frontier of particle physics for at least the next decade,
 1125 making it a unique tool with which to study particle physics. With the HL-LHC [2], high
 1126 statistics on rare particle physics processes will enable more precise measurements of param-
 1127 eters of the Standard Model and increase the sensitivity to signatures of physics beyond the
 1128 Standard Model [3]. To capitalize on the increased collision rate, the NSWs of the ATLAS
 1129 experiment must be replaced to keep the triggering and tracking performance [5].
 1130 Small-strip thin gap chambers are gas ionization chambers optimized for a high rate envi-
 1131 ronment [5]. Using the pad electrodes to define a region of interest makes it possible to get
 1132 track segments of ~ 1 mrad angular resolution quickly, which will be used as input to check

1133 if a collision originated from the interaction point and should be triggered on or not [5, 53].
1134 sTGCs are also able to provide better than 100 μm position resolution on each detector plane
1135 to fulfill precision offline tracking requirements [6].

1136 Ultimately, the positions of the sTGC strip electrodes need to be known in ATLAS to within
1137 $\sim 100 \mu\text{m}$ so that they can deliver the required position resolution. The ATLAS alignment
1138 system will position alignment platforms on the surface of the sTGC wedge, and an alignment
1139 model will be used to position the strips with respect to the alignment platforms [5]. Input
1140 to the alignment model comes from the datasets used to characterize the quadruplets. The
1141 x-ray method [8] is used to measure offsets of strips from their nominal position to achieve
1142 this goal. The alignment model could be built on x-ray data alone, but the sparseness of
1143 and large uncertainty on the local offsets mean that the alignment model could benefit from
1144 more input. Comparing the x-ray offsets to the CMM data [7] allows the effect of inter-layer
1145 misalignments to be isolated and increases the input to the alignment model.

1146 The cosmics dataset was used to confirm the local offsets measured with the x-ray gun. It
1147 provides relative local offsets between sTGC strip layers. The 2D visualizations of relative
1148 local offsets allow personnel to quickly identify areas of misaligned strips and make hypothe-
1149 ses of the physical origin of those misalignments. The correlation seen between the x-ray and
1150 cosmics residuals in quadruplets with large relative misalignments confirms the validity of
1151 the x-ray local offsets. Moreover, the mean of track residuals in an area can be used to make
1152 a robust estimation of the relative local offset, as shown by the estimation of systematic
1153 uncertainties; the relative local offsets for all two-fixed layer reference frames do not change
1154 by more than 100 μm given variation in data collection conditions and analysis algorithms.
1155 The cosmics relative local offsets are therefore relevant input for alignment studies and could
1156 improve the alignment model that will position each strip.

1157 Achieving the required position resolution on each layer of the NSWs in the particle track
1158 bending plane achieves the design momentum resolution for muons ejected towards the end-
1159 caps of ATLAS. Muons are important signatures of electroweak and Higgs sector events
1160 of interest for the ATLAS Collaboration’s future physics goals [5]. Being the second of two
1161 tracking technologies on the NSWs, an effective alignment model of sTGC quadruplets layers
1162 is a necessary part of making the NSWs redundant for 10 or more years of recording collisions
1163 in the High Luminosity era of the LHC.

¹¹⁶⁴ References

- ¹¹⁶⁵ [1] L. Evans and P. Bryant. LHC Machine. *Journal of Instrumentation*, 3(S08001), August 2008.
- ¹¹⁶⁶
- ¹¹⁶⁷ [2] G. Apollinari et al. High-Luminosity Large Hadron Collider (HL-LHC) Technical Design Report V. 0.1. Technical Report CERN-2017-007-M, CERN, Geneva, September 2017.
- ¹¹⁶⁸
- ¹¹⁶⁹ [3] A. Dainese et al. The physics potential of HL-LHC. In *Input to the European Particle Physics Strategy Update*, November 2018.
- ¹¹⁷⁰
- ¹¹⁷¹ [4] The ATLAS Collaboration. The ATLAS Experiment at the CERN Large Hadron Col-
¹¹⁷² linder. *Journal of Instrumentation*, 3(08):S08003, August 2008.
- ¹¹⁷³
- ¹¹⁷⁴ [5] T. Kawamoto et al. New Small Wheel Technical Design Report. Technical Report CERN-LHCC-2013-006, ATLAS-TDR-020, CERN, Geneva, June 2013.
- ¹¹⁷⁵
- ¹¹⁷⁶ [6] A. Abusleme et al. Performance of a Full-Size Small-Strip Thin Gap Chamber Prototype for the ATLAS New Small Wheel Muon Upgrade. *Nuclear Instruments and Methods in Physics Research Section A: Accelerators, Spectrometers, Detectors and Associated Equipment*, 817:85–92, May 2016. arXiv: 1509.06329.
- ¹¹⁷⁷
- ¹¹⁷⁸
- ¹¹⁷⁹ [7] E.M. Carlson. *Results of the 2018 ATLAS sTGC test beam and internal strip alignment of sTGC detectors*. M.Sc. thesis, University of Victoria, Victoria, Canada, 2019.
- ¹¹⁸⁰
- ¹¹⁸¹ [8] B. Lefebvre. Precision survey of the readout strips of small-strip Thin Gap Chambers using X-rays for the muon spectrometer upgrade of the ATLAS experiment. *Journal of Instrumentation*, 15(07):C07013–C07013, July 2020.
- ¹¹⁸²
- ¹¹⁸³
- ¹¹⁸⁴ [9] D.J. Griffiths. *Introduction to elementary particles*. Physics textbook. Wiley-VCH, Weinheim, Germany, 2., rev. ed., 5. reprint edition, 2011.
- ¹¹⁸⁵
- ¹¹⁸⁶ [10] M.E. Peskin and D.V. Schroeder. *An introduction to quantum field theory*. Addison-
¹¹⁸⁷ Wesley Pub. Co, Reading, Massachusetts, 1995.

- 1188 [11] P.A. Zyla et al. Review of Particle Physics. *PTEP*, 2020(8):083C01, 2020.
- 1189 [12] M. Kobayashi and T. Maskawa. CP-violation in the renormalizable theory of weak
1190 interaction. *Progress of theoretical physics*, 49(2):652–657, February 1973.
- 1191 [13] M.L. Perl et al. Evidence for Anomalous Lepton Production in $\{e\}^{\{+}\backslash ensuremath{-}\} \{e\}^{\backslash ensuremath{-}\}}$ Annihilation. *Physical Review Letters*, 35(22):1489–1492, De-
1192 cember 1975. Publisher: American Physical Society.$
- 1193
- 1194 [14] F. Englert and R. Brout. Broken Symmetry and the Mass of Gauge Vector Mesons.
1195 *Physical Review Letters*, 13(9):321–323, August 1964. Publisher: American Physical
1196 Society.
- 1197 [15] P.W. Higgs. Broken symmetries, massless particles and gauge fields. *Physics Letters*,
1198 12(2):132–133, September 1964.
- 1199 [16] D. Galbraith and C. Burgard. UX: Standard Model of the Stan-
1200 dard Model, November 2013. [http://davidgalbraith.org/portfolio/
1201 ux-standard-model-of-the-standard-model/](http://davidgalbraith.org/portfolio/ux-standard-model-of-the-standard-model/) last accessed on 2021-09-30.
- 1202 [17] C.A. Bertulani. *Nuclear physics in a nutshell*. In a nutshell. Princeton University Press,
1203 Princeton, N.J, 2007. OCLC: ocm85690422.
- 1204 [18] B.W. Carroll and D.A. Ostlie. *An introduction to modern astrophysics*. Pearson
1205 Addison-Wesley, San Francisco, 2nd ed edition, 2007. OCLC: ocm69020924.
- 1206 [19] M. Boezio and E. Mocchiutti. Chemical composition of galactic cosmic rays with space
1207 experiments. *Astroparticle Physics*, 39-40:95–108, December 2012.
- 1208 [20] The SNO Collaboration. Combined analysis of all three phases of solar neutrino data
1209 from the sudbury neutrino observatory. *Phys. Rev. C*, 88:025501, August 2013.
- 1210 [21] B. Pontecorvo. Neutrino Experiments and the Problem of Conservation of Leptonic
1211 Charge. *Soviet Physics—JETP*, 53:1717–1725, 1967.
- 1212 [22] S.M. Bilenky and S.T. Petcov. Massive neutrinos and neutrino oscillations. *Reviews of
1213 Modern Physics*, 59(3):671–754, July 1987.
- 1214 [23] B. Young. A survey of dark matter and related topics in cosmology. *Frontiers of Physics*,
1215 12(2):121201, April 2017.
- 1216 [24] C. Muñoz. Dark matter detection in the light of recent experimental results. *International
1217 Journal of Modern Physics A*, 19(19):3093–3169, July 2004.

- 1218 [25] G. Arnison et al. Experimental observation of isolated large transverse energy elec-
1219 trons with associated missing energy at s=540 GeV. *Physics Letters B*, 122(1):103–116,
1220 February 1983.
- 1221 [26] M. Banner et al. Observation of single isolated electrons of high transverse momentum
1222 in events with missing transverse energy at the CERN pp collider. *Physics Letters B*,
1223 122(5):476–485, March 1983.
- 1224 [27] G. Arnison et al. Experimental observation of lepton pairs of invariant mass around 95
1225 GeV/c² at the CERN SPS collider. *Physics Letters B*, 126(5):398–410, July 1983.
- 1226 [28] P. Bagnaia et al. Evidence for Z → e⁺e⁻ at the CERN pp collider. *Physics Letters B*,
1227 129(1):130–140, 1983.
- 1228 [29] The CDF Collaboration. Observation of Top Quark Production in $\bar{p}p$ Collisions with
1229 the Collider Detector at Fermilab. *Physical Review Letters*, 74(14):2626–2631, April
1230 1995. Publisher: American Physical Society.
- 1231 [30] The D0 Collaboration. Observation of the Top Quark. *Physical Review Letters*,
1232 74(14):2632–2637, April 1995. Publisher: American Physical Society.
- 1233 [31] The ATLAS Collaboration. Observation of a new particle in the search for the Standard
1234 Model Higgs boson with the ATLAS detector at the LHC. *Physics Letters B*, 716(1):1–
1235 29, September 2012. arXiv: 1207.7214.
- 1236 [32] The CMS Collaboration. Observation of a new boson at a mass of 125 GeV with the
1237 CMS experiment at the LHC. *Physics Letters B*, 716(1):30–61, September 2012. arXiv:
1238 1207.7235.
- 1239 [33] Standard Model Summary Plots June 2021, June 2021. <https://atlas.web.cern.ch/Atlas/GROUPS/PHYSICS/PUBNOTES/ATL-PHYS-PUB-2021-032/> last accessed on 2021-
1240 09-30.
- 1242 [34] O.S. Brüning et al. *LHC Design Report*. CERN Yellow Reports: Monographs. Geneva,
1243 2004.
- 1244 [35] ATLAS luminosity public results run-1, March 2011. <https://twiki.cern.ch/twiki/bin/view/AtlasPublic/LuminosityPublicResults> last accessed on 2021-09-20.
- 1246 [36] ATLAS luminosity public results run-2, July 2015. <https://twiki.cern.ch/twiki/bin/view/AtlasPublic/LuminosityPublicResultsRun2> last accessed on 2021-09-20.

- 1248 [37] The European Strategy for Particle Physics. Technical Report CERN/2685, CERN,
1249 2006. Adopted by the CERN council at a special session at ministerial level in Lisbon
1250 in 2006.
- 1251 [38] HiLumi HL-LHC Project. LHC/HL-LHC plan (last update january 2021). <https://hilumilhc.web.cern.ch/content/hl-lhc-project>, last accessed on 2021-09-09.
- 1252
- 1253 [39] M. Cepeda et al. Report from Working Group 2: Higgs Physics at the HL-LHC and
1254 HE-LHC. *CERN Yellow Reports Monographs*, 7:221–584. 364 p, Dec 2018.
- 1255 [40] ATLAS inner detector : Technical Design Report, 1. Technical Report CERN-LHCC-
1256 97-016, CERN, April 1997. ISBN: 9789290831020 Publication Title: CERN Document
1257 Server.
- 1258 [41] S. Haywood, L. Rossi, R. Nickerson, and A. Romanouk. ATLAS inner detector :
1259 Technical Design Report, 2. Technical Report CERN-LHCC-97-017, CERN, April 1997.
1260 ISBN: 9789290831037 Publication Title: CERN Document Server.
- 1261 [42] C. Grupen, B.A. Shwartz, and H. Spieler. *Particle detectors*. Cambridge University
1262 Press, Cambridge, UK; New York, 2008. OCLC: 1105536566.
- 1263 [43] ATLAS liquid-argon calorimeter : Technical Design Report. Technical Report CERN-
1264 LHCC-96-041, CERN, 1996. ISBN: 9789290830900 Publication Title: CERN Document
1265 Server.
- 1266 [44] ATLAS tile calorimeter : Technical Design Report. Technical Report CERN-LHCC-96-
1267 042, CERN, 1996. ISBN: 9789290830917 Publication Title: CERN Document Server.
- 1268 [45] The ATLAS Collaboration. ATLAS Muon Spectrometer: Technical Design Report.
1269 Technical Report CERN-LHCC-97-022, CERN, Geneva, 1997.
- 1270 [46] ATLAS magnet system : Technical Design Report, 1. Technical Report CERN-LHCC-
1271 97-018, CERN, April 1997. ISBN: 9789290831044 Publication Title: CERN Document
1272 Server.
- 1273 [47] The ATLAS Collaboration. Performance of the ATLAS muon trigger in pp collisions
1274 at $\sqrt{s} = 8$ TeV. *The European Physical Journal C*, 75(3):120, March 2015. arXiv:
1275 1408.3179.
- 1276 [48] S. Aefsky et al. The Optical Alignment System of the ATLAS Muon Spectrometer End-
1277 caps. *Journal of Instrumentation*, 3(11):P11005–P11005, November 2008. Publisher:
1278 IOP Publishing.

- 1279 [49] ATLAS level-1 trigger : Technical Design Report. Technical Report CERN-LHCC-98-
1280 014, CERN, August 1998. ISBN: 9789290831280 Publication Title: CERN Document
1281 Server.
- 1282 [50] A. Ruiz Martínez. The run-2 ATLAS trigger system. *Journal of Physics: Conference
1283 Series*, 762:012003, October 2016.
- 1284 [51] Technical Design Report for the Phase-II Upgrade of the ATLAS TDAQ System. Tech-
1285 nical Report CERN-LHCC-2017-020, ATLAS-TDR-029, CERN, Geneva, September
1286 2017.
- 1287 [52] P. Jenni, M. Nessi, M. Nordberg, and K. Smith. ATLAS high-level trigger, data-
1288 acquisition and controls : Technical Design Report. Technical Report CERN-LHCC-
1289 2003-022, CERN, July 2003.
- 1290 [53] E. Perez Codina. Small-strip Thin Gap Chambers for the muon spectrometer upgrade of
1291 the ATLAS experiment. *Nuclear Instruments and Methods in Physics Research Section
1292 A: Accelerators, Spectrometers, Detectors and Associated Equipment*, 824:559–561, July
1293 2016.
- 1294 [54] J. Townsend. *Electricity in gases*. Clarendon Press, Oxford, 1915.
- 1295 [55] S. Majewski, G. Charpak, A. Breskin, and G. Mikenberg. A thin multiwire chamber
1296 operating in the high multiplication mode. *Nuclear Instruments and Methods*, 217:265–
1297 271, 1983.
- 1298 [56] E. Gatti, A. Longoni, H. Okuno, and P. Semenza. Optimum geometry for strip cathodes
1299 or grids in MWPC for avalanche localization along the anode wires. *Nuclear Instruments
1300 and Methods*, 163(1):83–92, July 1979.
- 1301 [57] G. Battistoni et al. Resistive cathode transparency. *Nuclear Instruments and Methods
1302 in Physics Research*, 202(3):459–464, November 1982.
- 1303 [58] B. Lefebvre. *Characterization studies of small-strip Thin Gap Chambers for the ATLAS
1304 Upgrade*. PhD thesis, McGill University, Montreal, Canada, 2018.
- 1305 [59] P.K.F. Grieder. *Cosmic rays at Earth: researcher’s reference manual and data book*.
1306 Elsevier Science Ltd, Amsterdam, 1st ed edition, 2001.
- 1307 [60] R. Keyes et al. Development and characterization of a gas system and its associated
1308 slow-control system for an ATLAS small-strip thin gap chamber testing facility. *Journal
1309 of Instrumentation*, 12(04):P04027–P04027, April 2017.

- 1310 [61] Georgios Iakovidis. VMM3, an ASIC for Micropattern Detectors. Technical Report
1311 ATL-MUON-PROC-2018-003, CERN, Geneva, March 2018.
- 1312 [62] B. Chen. *Calibration Studies of the Front-End Electronics for the ATLAS New Small*
1313 *Wheel Project*. M.Sc. thesis, McGill University, Montreal, Canada, 2019.
- 1314 [63] R. Brun and F. Rademakers. ROOT: An object oriented data analysis framework. *Nu-*
1315 *clear Instruments and Methods in Physics Research Section A: Accelerators, Spectrome-*
1316 *ters, Detectors and Associated Equipment*, 389:81–86, 1997. See also ”ROOT” [software],
1317 Release 6.18/02, 23/08/2019, (<https://zenodo.org/record/3895860#.YVJW6n0pCHs>).
- 1318 [64] F. Sauli. Principles of operation of multiwire proportional and drift chambers. In *Cern*
1319 *Yellow Reports: Monographs*, page 92 p, Geneva, 1977. CERN, CERN. CERN, Geneva,
1320 1975 - 1976.
- 1321 [65] M. Hatlo et al. Developments of mathematical software libraries for the LHC experi-
1322 ments. *IEEE Transactions on Nuclear Science*, 52:2818–2822, 2005.
- 1323 [66] H. Guo. A Simple Algorithm for Fitting a Gaussian Function [DSP Tips and Tricks].
1324 *IEEE Signal Processing Magazine*, 28(5):134–137, September 2011.
- 1325 [67] I. Endo et al. Systematic shifts of evaluated charge centroid for the cathode read-out
1326 multiwire proportional chamber. *Nuclear Instruments and Methods in Physics Research*,
1327 188(1):51–58, September 1981.
- 1328 [68] B. Stelzer. The New Small Wheel Upgrade Project of the ATLAS Experiment. *Nuclear*
1329 *and Particle Physics Proceedings*, 273-275:1160–1165, April 2016.
- 1330 [69] X. Zhao et al. Cosmic test of sTGC detector prototype made in China for ATLAS
1331 experiment upgrade. *Nuclear Instruments and Methods in Physics Research Section A:*
1332 *Accelerators, Spectrometers, Detectors and Associated Equipment*, 927:257–261, May
1333 2019.

¹³³⁴ APPENDICES

₁₃₃₅ **Appendix A**

₁₃₃₆ **Uncertainty in cluster positions**

₁₃₃₇ The clusters were fit with Guo’s method [66] and Minuit2 for ROOT [65]. The difference in
₁₃₃₈ cluster means between the two algorithms is shown in figure A.1.

₁₃₃₉ The RMS of the distribution in figure A.1 is 57 μm , which is much larger than the statistical
₁₃₄₀ uncertainty in the mean for the Minuit2 algorithm, which peaks around 7 μm . An RMS of
₁₃₄₁ 60 μm is common for data taken with most quadruplets at 3.1 kV. Therefore, the uncer-
₁₃₄₂ tainty in the reconstructed cluster y -coordinate is assigned 60 μm due to variations in the
₁₃₄₃ reconstruction with different Gaussian fit algorithms.

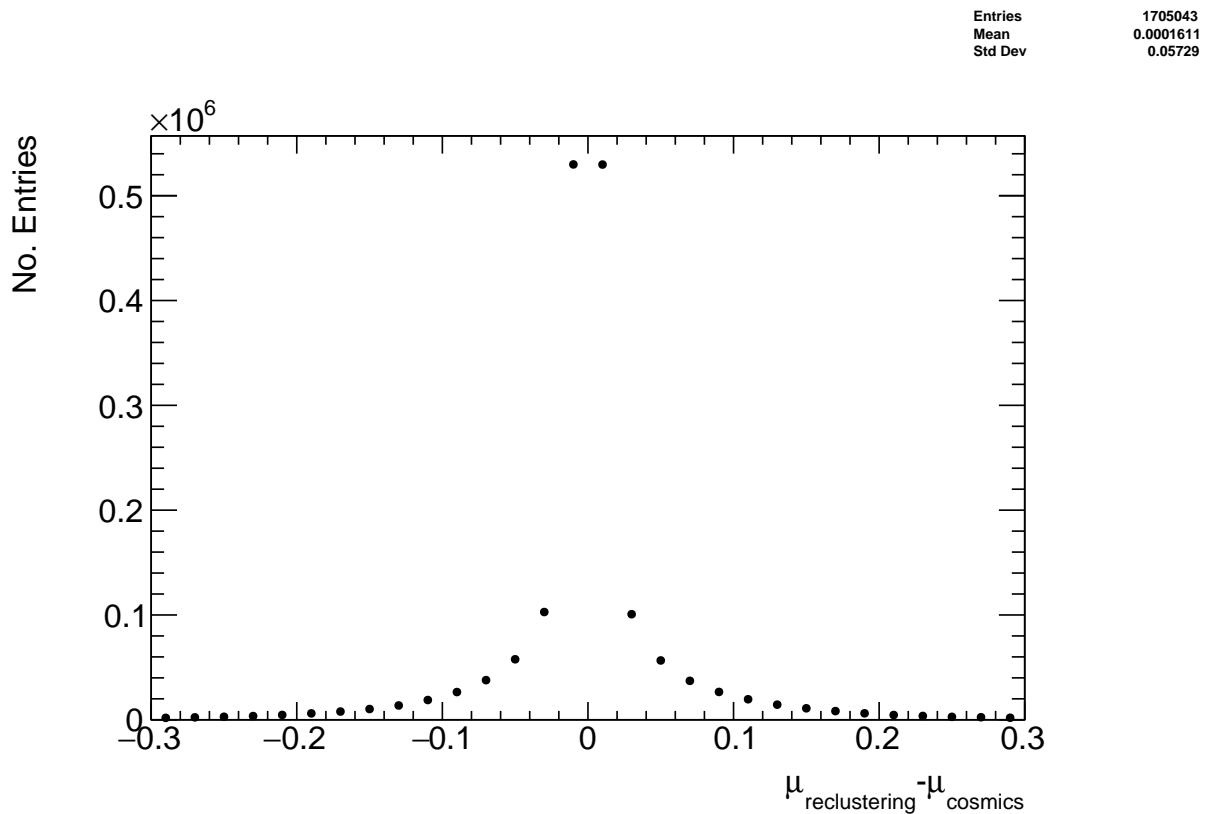


Figure A.1: The difference between cluster means calculated with Guo's method [66] in `tgc_analysis/CosmicsAnalysis` and `Minuit2` for `ROOT` [65] in `strip_position_analysis/ReClustering` for data collected with QL2.P.8 at 3.1 kV.

1344 **Appendix B**

1345 **Study of cosmics for alignment
1346 analysis statistical uncertainty**

1347 Typically, one million triggers (cosmic muon events, noise, photons and δ -rays) were collected
1348 for each Canadian quadruplet at McGill University, resulting in roughly half the number of
1349 viable tracks after cuts. For QS3.P.18, 3.5 million triggers were collected. To gauge the
1350 sensitivity of the analysis to the available statistics, partitions of this data with each with
1351 a different number of triggers were analyzed separately. Ultimately, the quantity of interest
1352 was the Gaussian mean of the residual distribution in regions of interest, so the peak in the
1353 distribution of the statistical uncertainty in the residual means for each area of interest for
1354 a specific tracking combination was used to gauge the quality of the analysis. How the peak
1355 in the residual mean uncertainty distribution changes with the number of triggers is shown
1356 in figure for tracks on layer 1 built from layers 3 and 4 [B.1](#).

1357 The uncertainty is already around 20 μm at 1 million triggers, suitable for distinguishing
1358 differences in offsets of order 50 μm as required. Although increased statistics could decrease
1359 the statistical uncertainty, it is not required for the goals of this analysis. Moreoever, the
1360 systematic uncertainty on the mean cosmics residuals is around 50 μm so the statistical
1361 uncertainty of 20 μm is nearly negligible.

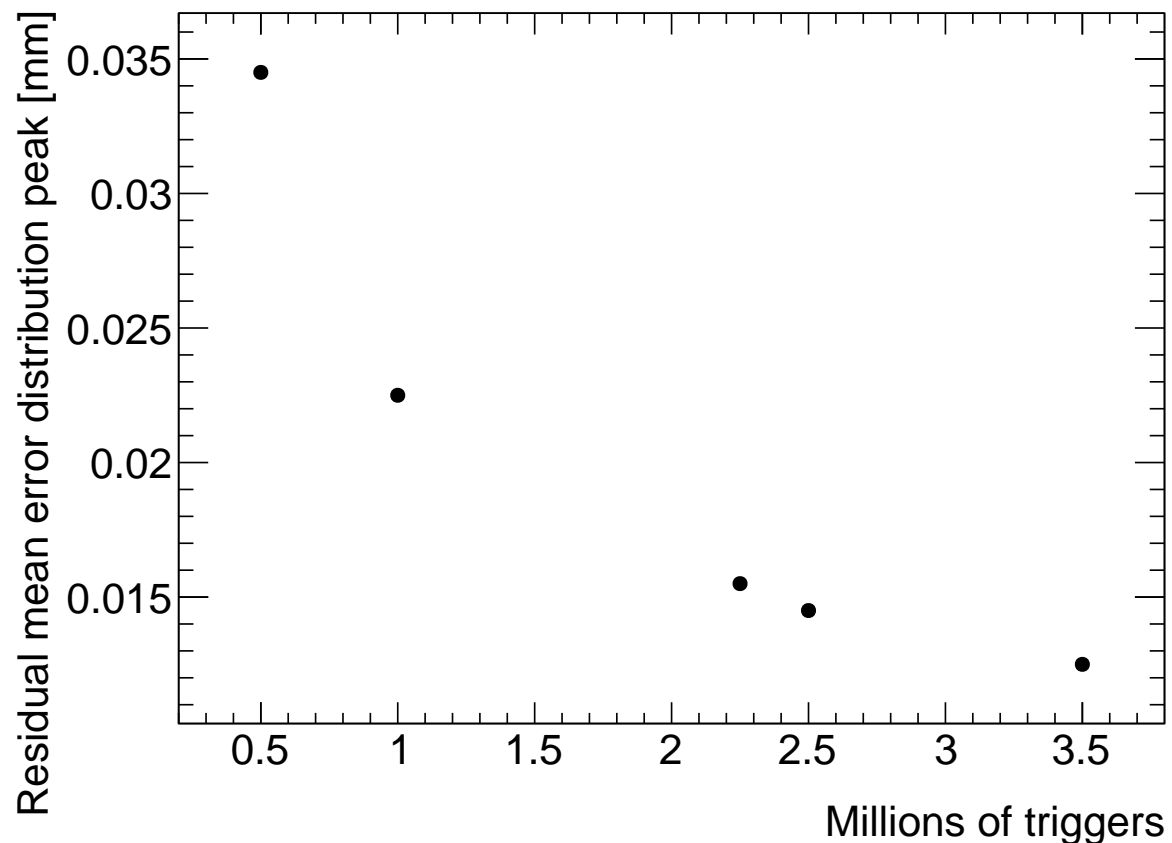


Figure B.1: How the peak of the distributions of uncertainties in the residual means in regions of interest for tracks on layer 1 built from layers 3 and 4 changed with the number of triggers used in the analysis. The distribution falls off as $\frac{1}{\sqrt{N}}$ as expected.

¹³⁶² Appendix C

¹³⁶³ Study of systematic uncertainties ¹³⁶⁴ when using cosmics data for ¹³⁶⁵ alignment studies

¹³⁶⁶ C.1 Residual distribution fit function

¹³⁶⁷ The distribution of residuals should be modeled by a double Gaussian fit[58]:

$$G(r) = A_s \exp\left[\frac{-(r - \mu)^2}{2\sigma_s^2}\right] + A_b \exp\left[\frac{-(r - \mu)^2}{2\sigma_b^2}\right] \quad (\text{C.1})$$

¹³⁶⁸ where r is the residual, A is the Gaussian amplitude, μ is the Gaussian mean, σ is the
¹³⁶⁹ Gaussian sigma, and the subscripts s and b stand for signal and background respectively.
¹³⁷⁰ One Gaussian captures the real (signal) tracks and the other captures the tracks built from
¹³⁷¹ noise (background). The Gaussian with the smaller width is identified as the signal.

¹³⁷² A single Gaussian fit failed less often than a double Gaussian fit. The Gaussian fits were
¹³⁷³ performed by initially estimating the amplitude to be 100 tracks, the Gaussian mean to be
¹³⁷⁴ the histogram mean, and Gaussian σ to be the RMS. The fit range was restricted to ± 1
¹³⁷⁵ root-mean-square (RMS) from the histogram mean. The modification helped the Gaussian
¹³⁷⁶ fit capture the signal peak. An example residual distribution is shown in figure C.1.

¹³⁷⁷ For all residual distributions in 100 mm by 100 mm bins on layer 4 built from clusters on
¹³⁷⁸ layers 1 and 2, the difference in Gaussian and double Gaussian means and σ 's is shown in
¹³⁷⁹ figure C.2a. The mean of the distribution is centered around zero (within the RMS of the

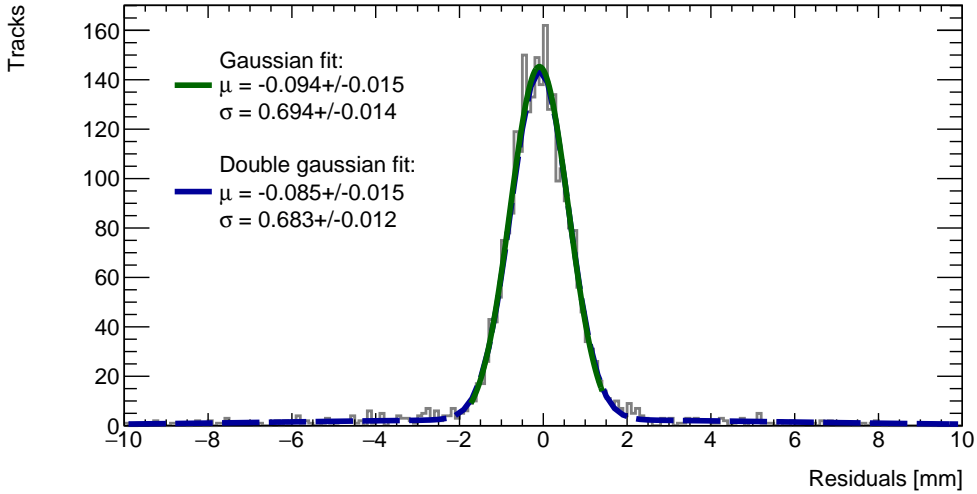
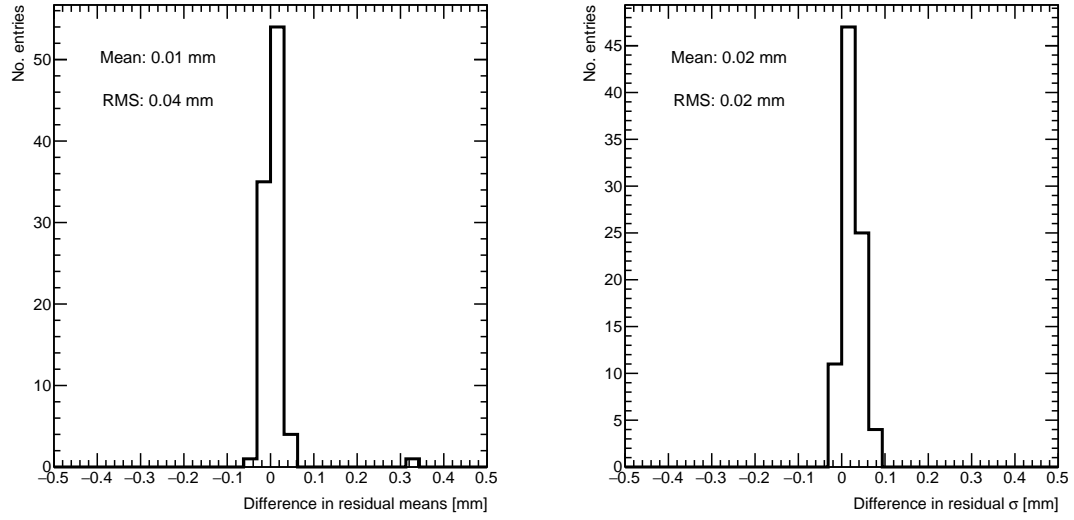


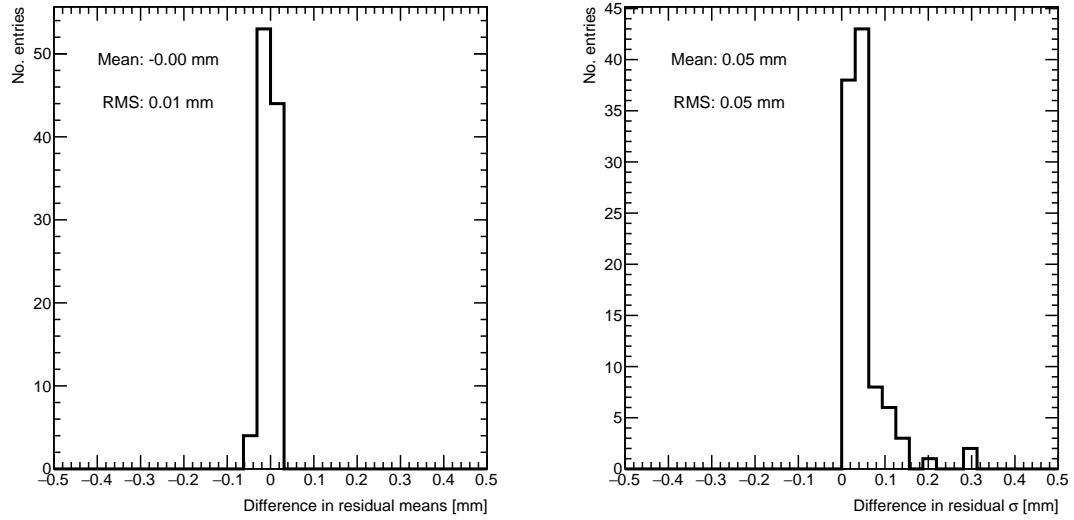
Figure C.1: Residual distribution for track residuals on layer 4 built from clusters on layers 1 and 2 for $x \in [-3.00, 97.00]$ mm, $y \in [394.60, 494.60]$ mm, fit with a double Gaussian and a single Gaussian in a range of ± 1 RMS from the histogram mean.

1380 distribution) so the choice of fit algorithm imbues no measurable bias. The order of the
1381 RMS is such that the difference in residual means at 40 μm is just significant, so it should
1382 be accounted for as a systematic uncertainty on the Gaussian residual means. The 40 μm
1383 RMS is for the tracking combination with the worst extrapolation lever arm and the widest
1384 distribution of mean differences; the interpolation combinations have narrower distributions,
1385 as shown in figure C.2b. The RMS of the distribution for residual means on layer 2 obtained
1386 using reference layers 1 and 3 is only 10 μm , which is almost negligible.

1387 The Gaussian σ should be larger than the double Gaussian σ because the Gaussian distri-
1388 bution includes the effect of the noise tracks that can yield large residuals, while the double
1389 Gaussian models signal and background residuals separately. For this analysis, only the
1390 residual mean was important, so the systematic overestimate of the signal σ in the Gaussian
1391 fit shown in the right-side plots of figure C.2 was allowed.



(a) Difference in residual distribution means (left) and σ 's (right) extracted with a Gaussian and double Gaussian fit, for all residual distributions in 100 mm by 100 mm bins on layer 4 built from clusters on layers 1 and 2 for sample quadruplet QL2.P.8.



(b) Difference in residual distribution means (left) and σ 's (right) for a Gaussian and double Gaussian fit, for all residual distributions in 100 mm by 100 mm bins on layer 2 built from clusters on layers 1 and 3 for sample quadruplet QL2.P.8.

Figure C.2

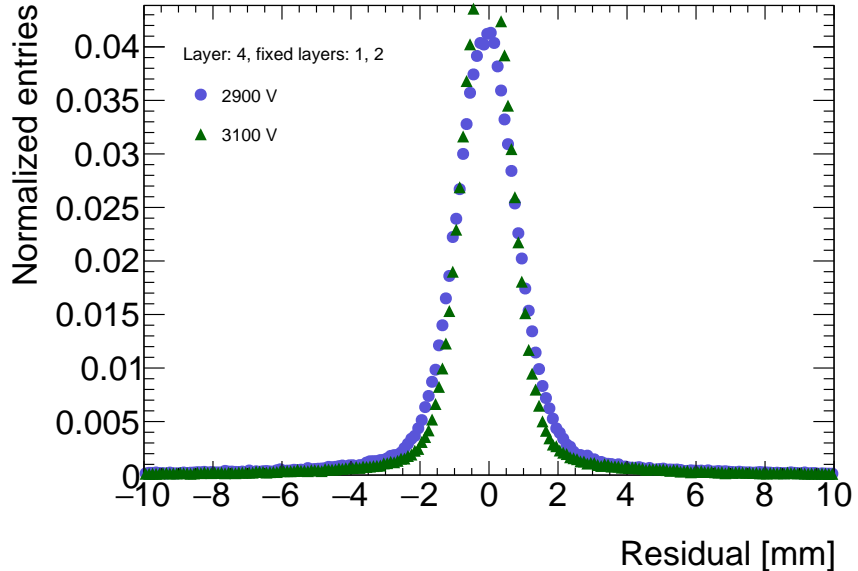


Figure C.3: Residual distribution for tracks on layer 4 built from clusters on layers 1 and 2 for sample quadruplet QL2.P.8 for data collected at 2.9 kV and 3.1 kV.

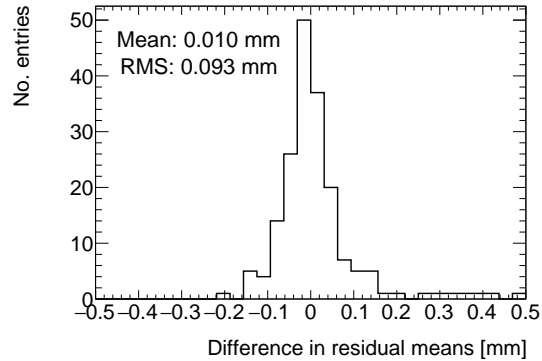
1392 Ultimately, a Gaussian fit was chosen for the track residual distributions because it was more
1393 robust and did not affect the fitted mean values too strongly.

1394 C.2 Cosmic muon data collection voltage

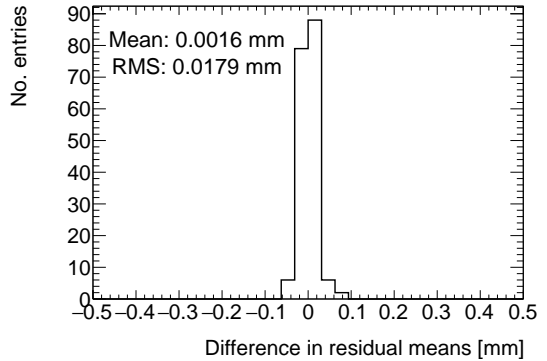
1395 Cosmic muon data was collected at 2.9 kV and 3.1 kV because although 2.9 kV is closer to
1396 the operating conditions the chambers will be subject to in ATLAS, the extra gain provided
1397 by operating at 3.1 kV increased the signal to noise ratio for pad signals. Also, the tracking
1398 efficiency was higher with data collected at 3.1 kV. As such, cosmic muon data collected at
1399 3.1 kV was used in the analysis presented in the body of the thesis.

1400 The difference in gain affects the relative population of clusters of different sizes, which in
1401 turn affects the uncertainty in the mean cluster positions on each layer, the uncertainty in
1402 the track positions and the residual distributions. The residual distributions for 3.1 kV data
1403 are narrower, as shown in figure C.3.

1404 Neither dataset is better for calculating the mean of residuals in a given area, so a systematic
1405 uncertainty can be assigned based on the difference in residual means calculated for 2.9 kV
1406 and 3.1 kV data per tracking combination. For each tracking combination, the difference



(a) Difference in residual means when measured with residuals on layer 4 built from clusters on layers 1 and 2.



(b) Difference in residual means when measured with residuals on layer 2 built from clusters on layers 1 and 3.

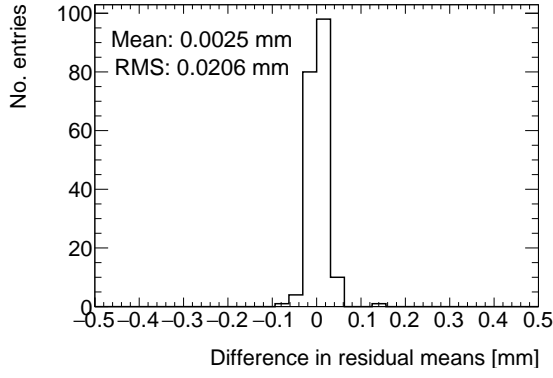
Figure C.4: Difference in residual means for data collected with sample quadruplet QL2.P.8 at 2.9 kV and 3.1 kV respectively in 100 mm by 100 mm bins.

1407 in the fitted track residual means in 100 mm by 100 mm areas for 2.9 kV and 3.1 kV data
 1408 are put in a distribution for a sample quadruplet, as shown in figure C.4. The means of
 1409 the distributions for both tracking combinations are near zero, so as expected the collection
 1410 voltage introduces no bias. Tracks built from clusters on layers 1 and 2 and extrapolated to
 1411 layer 4 have the worst lever arm and hence the largest root-mean-square (RMS) of 100 μm .
 1412 The width of the distributions for geometrically favourable tracking combinations are much
 1413 narrower. The narrowest width of the residual mean difference distribution is for tracks on
 1414 layer 2 built from clusters on layers 1 and 3 (see figure C.4b), with a value of 20 μm .

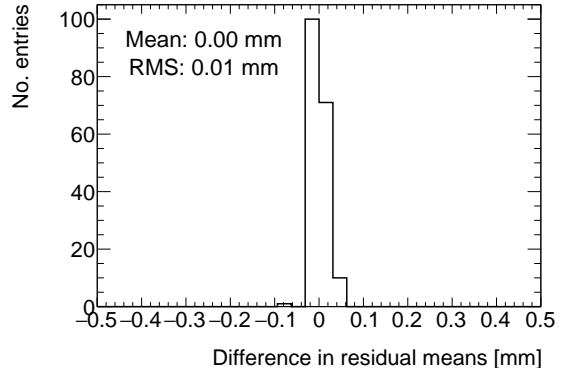
1415 C.3 Cluster fit algorithm

1416 To ensure that changing the cluster fitting algorithm like in appendix A would not change
 1417 the calculated mean of residuals in each region of interest significantly, the residual means
 1418 were compared in both cases. The distribution of the difference in residual means is plotted
 1419 in figure C.5 for the tracking combinations with the worst and most favourable extrapolation
 1420 lever arms.

1421 The mean of the distributions are centered around zero, so the choice of cluster fit algorithm
 1422 did not introduce any bias. Differences on the order of 50 μm are important, so the root-
 1423 mean-squares (RMS's) of the distributions show that the clustering algorithm had a small
 1424 but notable effect between 10-20 μm from the most to least geometrically favourable tracking



(a) Difference in residual means when measured with residuals on layer 4 built from clusters on layers 1 and 2.



(b) Difference in residual means when measured with residuals on layer 2 built from clusters on layers 1 and 3.

Figure C.5: Difference in residual means when the cluster fit algorithm is `Minuit2` [65] versus Guo's method [66] for two different tracking combinations for sample quadruplet, QL2.P.8.

combinations. Therefore, the RMS for each tracking combination will be used to add a systematic uncertainty on the residual means accounting for the effect that different cluster fit algorithms have on the residual means.

C.4 Differential non-linearity

Definition

In this context, differential non-linearity (DNL) is when the reconstructed cluster mean is biased by the fit of the discretely sampled peak signal amplitude distribution over the strips. The bias depends on the relative position of the avalanche with respect to the center of the closest strip. For a summary of DNL, refer to page 40 of [58], an early paper studying its effects [67], and for an example application, refer to [6].

Application and effect of DNL

The cluster mean was corrected for DNL using the equation:

$$y' = y + a \sin(2\pi y_{rel}) \quad (\text{C.2})$$

where y is the cluster mean, y_{rel} is the relative position of the cluster mean with respect to the strip's center, a is the amplitude of the correction, and y' is the corrected cluster

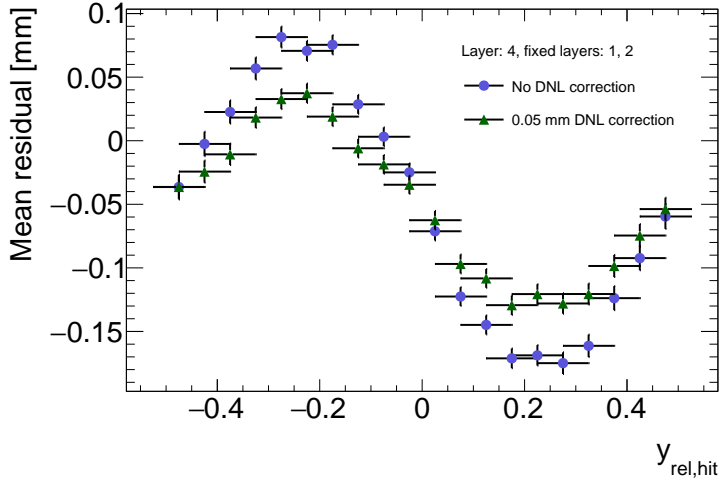


Figure C.6: Effect applying a 50 μm DNL correction to the profile of the residuals sorted by y_{rel} for residuals built from clusters on layers 1 and 2 and extrapolated to layer 4 of quadruplet, QL2.P.8.

mean. The amplitude can be derived by comparing the reconstructed hit position to the expected hit position, as done in [6]. With cosmic muons, there is no reference hit position to compare to, so track residuals were used as a proxy [58]. The hallmark of the DNL effect is the periodic pattern in the residual versus y_{rel} profile, and the effect of correcting the cluster means using an amplitude of 50 μm is shown in figure C.6. An amplitude of 50 μm is based on Dr. Lefebvre's [58] estimate of the DNL amplitudes by layer, quadruplet and cluster size using cosmic muon tracks [58]. Little variation is seen in the amplitude parameters with respect to the quadruplet tested, the layer and the cluster size so a universal correction is used.

Although the correction is not large enough in this case, the figure shows that the correction does reduce the DNL effect. Slightly better performance is seen in the interpolation tracking combinations where the quality of the residuals is better. DNL corrections for cosmic muon data are difficult because the DNL effect is obscured by the effect of misalignments between strip layers and noise. Misalignments cause the center of the sinusoidal pattern in figure C.6 to be shifted off of zero, since the mean of residuals is shifted.

Figure C.7 shows the distribution of the difference in residual means calculated in 100 mm by 100 mm areas for mean track residuals on layer 4 obtained using layers 1 and 2 as reference. The mean of the distribution is zero within the root-mean-square so the DNL correction does not bias the residual means. It is apparent that the effect of the DNL correction on

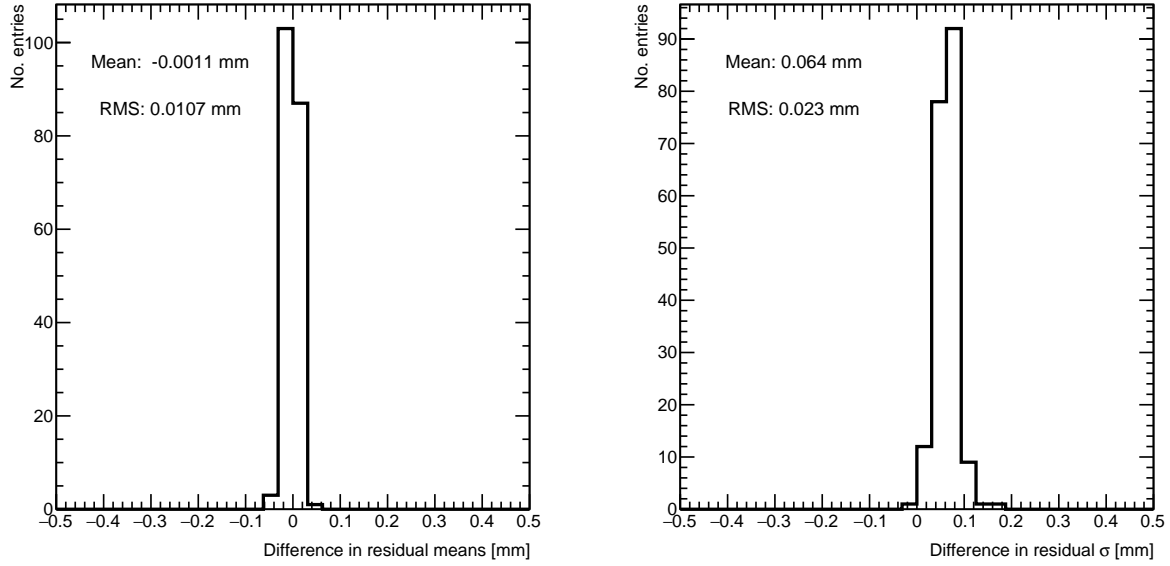


Figure C.7: Difference in residual distribution means and σ 's with and without DNL correction for residuals on layer 4 obtained using reference layers 1 and 2 for sample quadruplet, QL2.P.8.

the residual means is on the order of micrometers given the RMS of $10 \mu\text{m}$ in the worst extrapolation case. Although the σ 's of the residual distributions shrink with the DNL correction, the mean is the parameter of interest so the bias in the fitted σ 's was ignored. Therefore, in this analysis DNL is not corrected for.

₁₄₆₂ Appendix D

₁₄₆₃ Printable plots

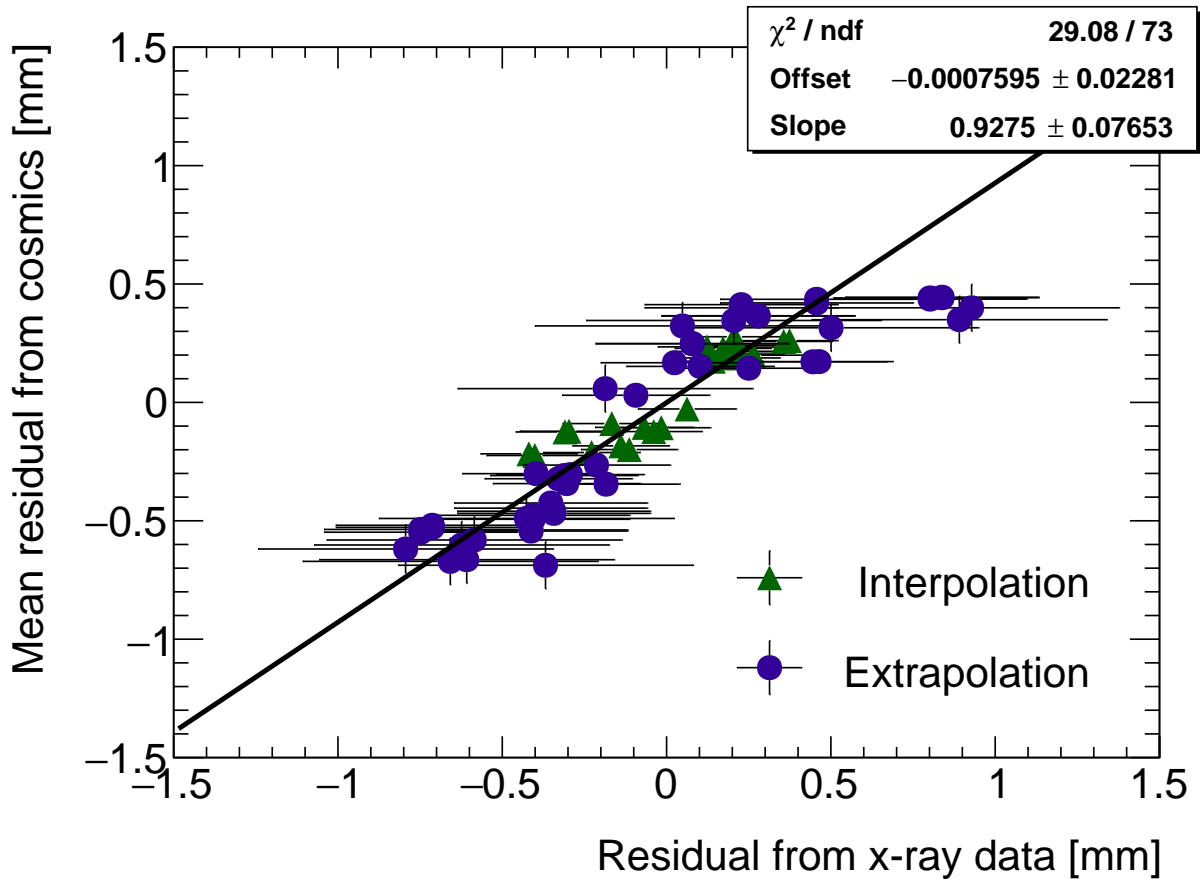


Figure D.1: Correlation plot between x-ray and cosmics residuals for all tracking combinations for QL2.P.11. Each rectangle is centered on an x-ray and mean cosmics residual pair. The width of the rectangles in x and y are the uncertainty in the x-ray and mean cosmics residual respectively. This is a printable version of figure 7.2 in section 7.1.

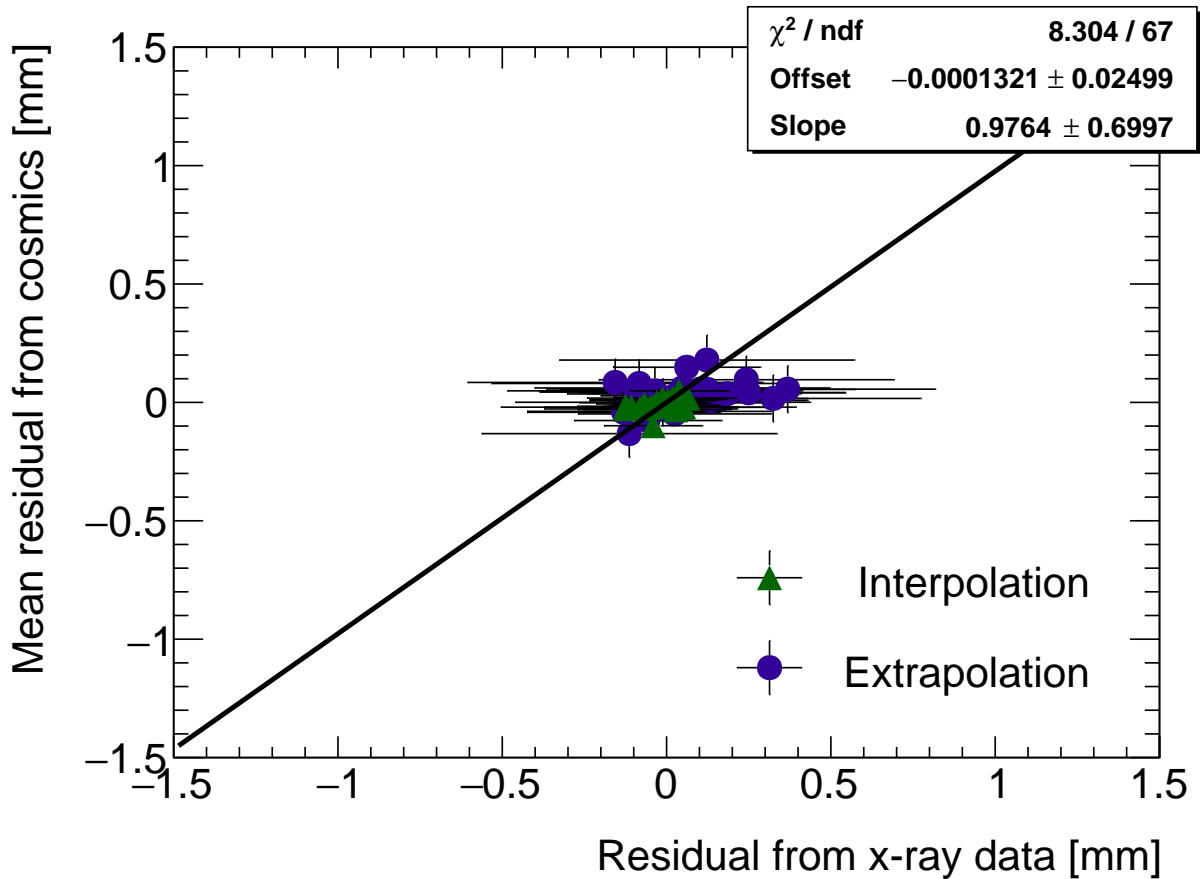


Figure D.2: Correlation plot between x-ray and cosmics residuals for all tracking combinations for QL2.P.8. Each rectangle is centered on an x-ray and mean cosmics residual pair. The width of the rectangles in x and y are the uncertainty in the x-ray and mean cosmics residual respectively. This is a printable version of figure 7.3 in section 7.1.